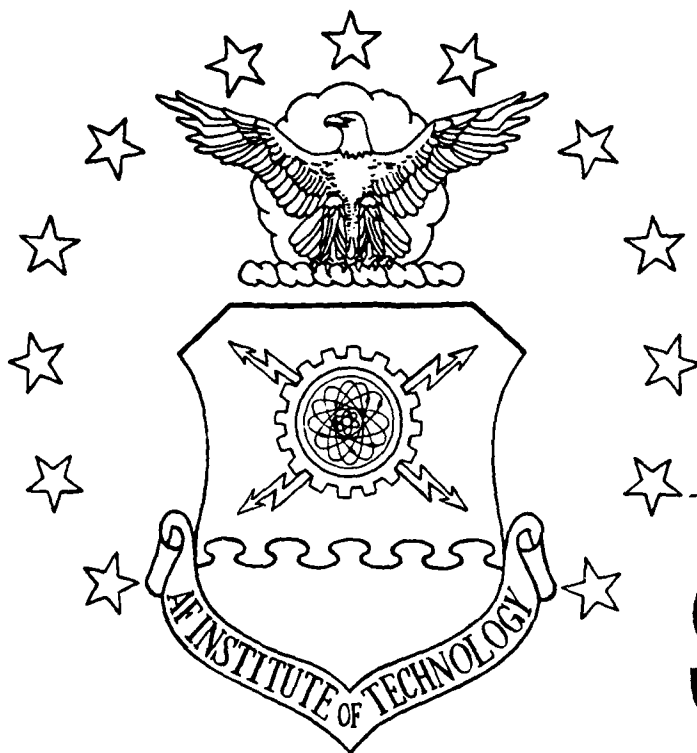①

DTIC
S ELECTE
DEC 15 1989
B D

FRACTAL GEOMETRY SEGMENTATION
OF POLARIMETRIC
SYNTHETIC APERTURE RADAR IMAGES

THESIS

Mark Allen Maneely
Captain, USAF

AFIT/GE/ENG/89D-28

S

DEPARTMENT OF THE AIR FORCE
AIR UNIVERSITY

AIR FORCE INSTITUTE OF TECHNOLOGY

Wright-Patterson Air Force Base, Ohio

89 12 15 048

FRACTAL GEOMETRY SEGMENTATION
OF POLARIMETRIC
SYNTHETIC APERTURE RADAR IMAGES

THESIS

Presented to the Faculty of the School of Engineering

of the Air Force Institute of Technology

Air University

In Partial Fulfillment of the

Requirements for the Degree of

Master of Science in Electrical Engineering

Mark Allen Maneely, B.S.E.E

Captain, USAF

December, 1989

Acknowledgments

I am deeply indebted to my thesis advisor Lt Col David E. Meer for the technical and personal support he provided throughout my thesis efforts. I am also thankful to my thesis committee members, Dr Matthew Kabrisky and Maj Phil Amburn for their inputs and aid.

I thank my thesis sponsor, Dr Ed Zelnio, and his office for their support.

I also thank Captain Ron Jackson for his programming expertise in authoring the image generation program used in this thesis.

I am especially grateful to the AFIT computer systems manager, Mr Dan Zambon, for his undying patience and professionalism. Without his assistance and support I could not have completed this thesis.

<div align="right">Mark Allen Maneely</div>

Accession For	
NTIS GRA&I	☑
DTIC TAB	☐
Unannounced	☐
Justification	
By	
Distribution/	
Availability Codes	

Dist	Avail and/or Special
A-1	

Table of Contents

List of Figures

List of Tables

AFIT/GE/ENG/89D-28

Abstract

This thesis describes how fractal geometry was used to segment synthetic aperture radar (SAR) images. The fractal dimension of each non-overlapping 8x8 pixel region in a 512x512 pixel image was estimated by use of a multidimensional extension of the box counting algorithm. The differences in estimated fractal dimensions were used to differentiate between regions. The SAR images used were represented by quantized "surfaces". These surfaces were defined by nine different datasets of various Euclidean dimensions ranging from three to five. The degrees of freedom (Euclidean dimensions) of the datasets were the X and Y coordinates of each pixel and various combinations of power return values, magnitude return values and phase return values for each pixel. The SAR return values for four different SAR transmit and receive polarization configurations were determined by polarization synthesis techniques using the Stokes vectors of the transmitted and backscattered waves and the target reflectivity phase matrix. Phase matrix data for three different scenes was provided by the Jet Propulsion Laboratory, Pasadena, CA.

Thesis results indicate that the fractal dimension of an image "surface" provides a useful method to segment SAR images. Comparisons between segmentations made using various datasets indicate that datasets containing the magnitude and phase return values yield more information helpful to image segmentation than do datasets containing only power return values. It was also determined that combinations of the various types of return values (ie. power, magnitude and phase returns) into a single dataset of higher Euclidean dimension, can lead to better segmentations than those made using lower dimensional datasets. The fractal dimension estimation and segmentations techniques used in this thesis are not unique to SAR imagery. They may be easily applied to any data which can be arranged into datasets representing image "surfaces."

FRACTAL GEOMETRY SEGMENTATION
OF POLARIMETRIC
SYNTHETIC APERTURE RADAR IMAGES

I. Introduction

1.1 Overview

This chapter provides a brief discussion of the general image segmentation and object identification problem and presents one potential approach to solving this problem using fractal geometry. The proposal for this thesis, including the basic assumptions, thesis scope, evaluation criteria and expected gain is also presented. A list of necessary support equipment, both hardware and software is included. This chapter concludes with a brief description of the content of each of the following chapters.

1.2 Background

Identification and classification of Synthetic Aperture Radar (SAR) images is of particular interest to the United States Air Force. The computer automation of this identification process requires mathematical descriptions of the objects (images) of interest. Several methods currently exist of modelling objects using a relatively new mathematical science called fractal geometry.

Synthetic Aperture Radar "is an airborne (or spaceborne) radar mapping technique for generating high resolution maps of surface target areas and terrain." [15:185] As such, most SAR images contain both natural and man-made objects. It is hypothesized that the fractal dimensions of these natural objects are distinct from those of man-made objects. Further, it is theorized that complex polarimetric data collected by the SAR which is usually discarded during the generation of SAR images may hold some information helpful to object identification.

1.3 Problem

The specific purpose of this thesis is two-fold.

1. Determine if the use of fractal dimension is a valid criteria for distinguishing features and objects in SAR images.

2. Determine if use of full polarimetric data aids in the process of feature segmentation and identification in SAR images.

1.4 Assumptions

"Fractal geometry provides both a description and a mathematical model for many of the seemingly complex forms found in nature." [4:1] It is this property of fractals which stimulates such great interest in their study. Alex Pentland's experiments using fractals as models of nature led him to conclude "that fractal-based segmentation will likely prove a general and powerful technique." [22:671] It is this hypothesis upon which the work in this thesis is based.

1.4.1 Fractal Model of Nature.
The most basic assumption upon which this research effort is based is that objects can be modelled by fractal sets. While this premise is certainly supported by the literature [4] [5] [8] [20] [17] [22] [27] [35], its validity for this thesis will only be proven in the thesis final results.

1.4.2 Images Model the Scene.
A second major assumption is that the images of natural scenes contain the information necessary to make conclusions about the scene itself. Pentland found in his research that "... we can estimate the fractal dimension of the surface by measuring the fractal dimension of the image." [22:664]

1.4.3 Spatial Invariance of Fractal Model.
This thesis also assumes that the measured fractal dimension of the images is independent of both scale and orientation. The validity of this assumption follows directly from the definition of self similarity of a fractal set. It is further supported by Pentland's observations that a linear transformation (rotation or translation) of a fractal set is a fractal set with the same fractal dimension [22:665]

and that in his experiments the computed fractal dimension of natural scenes was "always stable over at least 4:1 variations of scale; most segmentations were stable over a range of 8:1." [22:668]

1.5 Scope

This thesis proposed to differentiate between natural and man-made objects and between different naturally occurring regions by determining the distribution of fractal dimensions within the SAR images. Initially, this methodology was applied for a dataset consisting of the power return values used in conventional SAR analysis. The same technique was then applied for each of the possible co-polarized and cross-polarized datasets and various combinations of complex polarimetric data.

1.6 Evaluation Criteria

The validity and quality of this segmentation technique was both a subjective determination by the author and his thesis advisor and committee and an objective analysis based on the technique's ability to differentiate between areas of interest within the SAR images. The subjective determination was made after visually comparing the segmented imag.s to the original SAR images and making a determination of the accuracy and utility of the fractal segmenting technique based on a priori knowledge about the objects and scenes depicted in the original images. The objective analysis judged the quality of the segmentations based on comparisons of a calculated figure of merit.

1.7 Support Equipment

The following equipment, software and materials were required for this thesis. All were resident in the AFIT Signal Processing Laboratory located in Building 641.

- MicroVax II Workstation with tape drive.

- MicroVMS 4.4 Operating System.

    - VAX FORTRAN V5.0 Compiler.

– MATRIXx V2.0 Software package.

The Jet Propulsion Laboratory, California Institute of Technology, Pasadena, CA, provided the polarimetric SAR data.

1.8 Additional Support

This thesis was sponsored by Dr. Edmund G. Zelnio, Chief of Technology Group, Wright Research Development Center, Wright Patterson, AFB, OH. (Office symbol: AARA - 2. Telephone Number: 255-3050, AV 785-3050)

1.9 Conclusion and Expected Gain

If the fractal geometry method of segmentation is valid, then results of this thesis will be useful as an automated data reduction technique in the interpretation of SAR images. If the interpretation of images containing full polarimetric data provides information helpful to object identification, this thesis will also present a "better" object identification technique than those currently employed for analyzing SAR images.

1.10 Remaining Chapters

Chapter II of this thesis presents the background, definition and description of fractal geometry. It includes examples of fractal sets and explanations of the properties of fractals relevant to this thesis.

Chapter III describes Synthetic Aperture Radar (SAR). It contains explanations of why and how SAR is used and how polarimetric data is obtained. It also contains a brief description of the equipment and algorithms used by JPL to collect the data used in this thesis.

Chapter IV contains the thesis methodology. Herein is explained the methods chosen to solve the problems of estimating the fractal dimensions of SAR images and how these images were displayed and segmented.

Chapter V contains the results and analysis of the thesis methodology.

Chapter VI is the thesis conclusion. It also presents the author's recommendations for further studies in this area.

A supplement to this thesis is available through AFIT/ENG. It includes listings of all of the FORTRAN programs used in this thesis and an Operating Guide for the use of the datasets and the FORTRAN programs. Distribution of the thesis supplement is restricted to DOD personnel only.

II. Fractal Geometry

2.1 Overview

This chapter provides a definition, background and explanation of the properties of fractals. It includes a rationale for the study of this new geometry and its potential applications.

2.2 Background

Benoit B. Mandelbrot coined the term "fractal" and developed a new "geometry of nature," called fractal geometry, in the 1970's [20:4]. This new field provided an arena for the study of a variety of curves and shapes that, after their original discovery, were discarded for decades simply because they could not be explained by the rules of classical Euclidean geometry. Examples from this "gallery of monsters" are continuous but non-differentiable curves [3:2], the Peano space filling curve [17:3], Cantor dusts [17:74], and traces of physical Brownian motion [17:12].

2.3 Definition

Mandelbrot defines a fractal as "a set for which the Hausdorff Besicovitch dimension strictly exceeds the topological dimension." [17:15] This is denoted $D_f > D_t$, where D_f is the "fractal dimension" and D_t is the "topological dimension."

Topological dimension is a rigorous mathematical term which generally corresponds to our intuitive sense of Euclidean dimension. For example, a shape containing only disjoint points (a dust) has a topological dimension of zero, a continuous curve or line has D_t equal to one, a surface has D_t equal to two, and a volume has a D_t of three. Although topological dimension is always an integer, the dimension of a fractal need not be an integer [17:15]. The fractal dimension provides an objective means for comparing and contrasting fractals [4:172]. It also provides a subjective feel for the "density" [4:172], "roughness" [22:662], or "wiggliness" [35:6] of a curve or surface.

2.4 Self Similarity

Perhaps the most important and useful property of fractals is that of self similarity.

When each piece of a shape is geometrically similar to the whole, both the shape and the cascade that generate it are called self similar. [17:34]

It is this property of fractals that distinguishes them most from the shapes of conventional Euclidean geometry. Simply stated, a self similar fractal is identical to itself regardless of the reference scale in which it is observed [35:17]. This property makes fractals extremely useful in overcoming the general pattern recognition problems associated with translation, scaling and rotation [14:59].

A self similar fractal can be thought of as "a set of N copies of itself (with possible translations and rotations), each of which is scaled by a factor, r, from the whole" [35:17]. Using this property, the fractal dimension (also called similarity dimension) is given by [17:44]

$$D_f = \frac{\ln(N)}{\ln(\frac{1}{r})} \tag{2.1}$$

where

D_f = the fractal dimension

N = the number of self similar subintervals of the fractal

r = the length of each of the subintervals

(assumes the total length of the fractal is normalized to one)

Equation 2.1 is helpful when building a fractal set with a specific desired dimension. The size and number of the parts of the fractal will be determined by this equation. Conversely, Equation 2.1 can also be used to make a rough estimate of the fractal dimension of an existing fractal set. By counting and measuring the size of the parts of this fractal, and using these as estimates for N and r, an estimate of D_f can be calculated.

2-2

A more accurate estimate of the fractal dimension of an existing set however, is given by [4:177].

$$D_f = \lim_{\frac{1}{r} \to 0} \frac{\ln(N)}{\ln(\frac{1}{r})} \qquad (2.2)$$

Equation 2.2 is often used instead of Equation 2.1 to help estimate the fractal dimension of fractal set. However, this thesis makes use of Equation 2.1 when making these estimates. The rationale behind this decision is included in Chapter IV.

2.5 Fractal Dimension Estimation

Although its accuracy may not be the best possible, Equation 2.1 does provide a resonable method for estimating the fractal dimension of a curve or surface. For example, in Figure 2.1, the line segment is composed of five identical subintervals each having length equal to one-fifth of the whole, therefore $1/r$ is equal to five, and $D_f = \ln(5)/\ln(5)$, or one. The fractal dimension of this set is consistent with the intuitive sense of Euclidean dimension of a line.
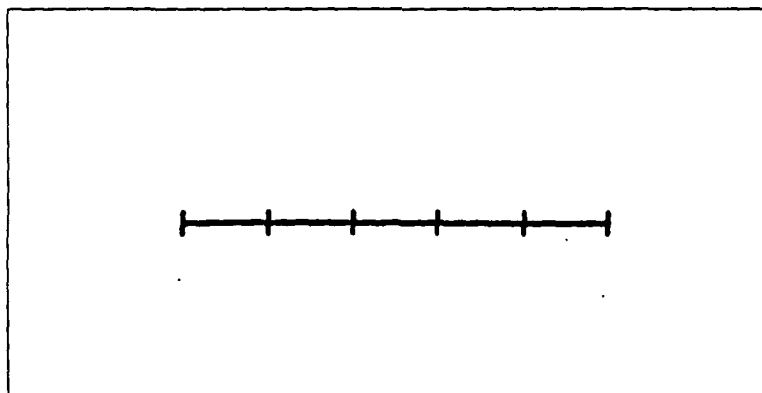
Figure 2.1. Self Similiar Line Segment [17:34]

For the self similar Triadic Koch Curve, shown in Figure 2.2 in four stages of evolution, N is equal to four, $1/r$ is three, therefore $D_f = \ln(4)/\ln(3)$, or approximately 1.26 [13:Chap 2-4]. The Koch curve is generated by starting with a line segment of unit length. The middle one-third of this line is then removed and replaced by two line segments of the same length which form an equalateral triangle with the original middle segment. This

remove and replace process is then repeated for every remaining line segment ad infinitum. The Koch curve is more "wiggly" than the line segment of Figure 2.1 therefore its expected fractal dimension is greater than one.
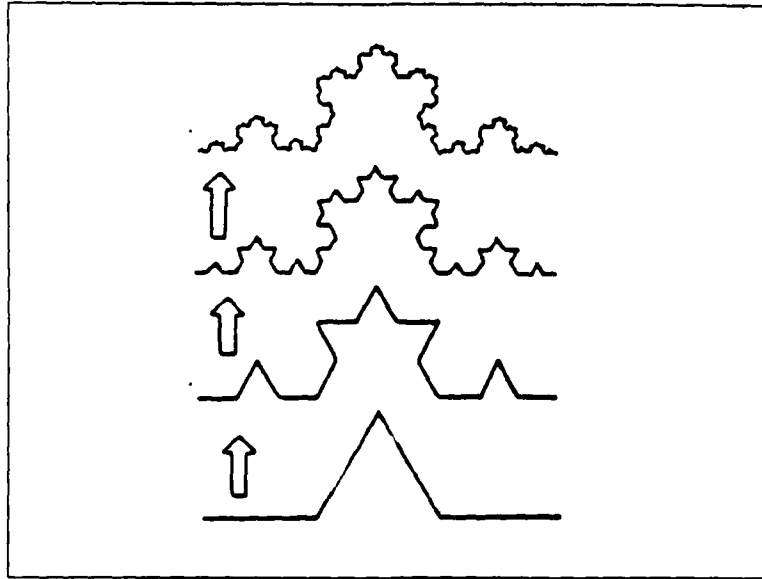
Figure 2.2. Triadic Koch Curve [15:29]

N is equal to two and $1/r$ is equal to three for the Triadic Cantor Dust, shown in Figure 2.3, also shown in four stages of evolution, thus $D_f = \ln(2)/\ln(3)$, or approximately 0.63. The Cantor Dust is generated by starting with a line segment of unit length. The middle one-third of this segment is then removed. Then the middle one-third of each of the remaining line segments is removed. This process is repeated ad infinitum. The Cantor dust is a set which is more than a single point (it is actually of collection of "points"), but it is less than the line segment from which it originated. Therefore its expected fractal dimension is between zero and one.

In this manner, Equation 2.1 can be used to estimate the fractal dimension of an object or shape that exhibits some self similarity over, at least, a small range of scaling. This same method, extended in a 2-dimensional Euclidean sense, allows two other methods of estimating the fractal dimension. These are the Closed Ball estimation and the Box Counting estimation [4:174-177]. For these two methods the fractal subintervals are no longer line segments, but are now taken to be circles or squares, respectively. A further
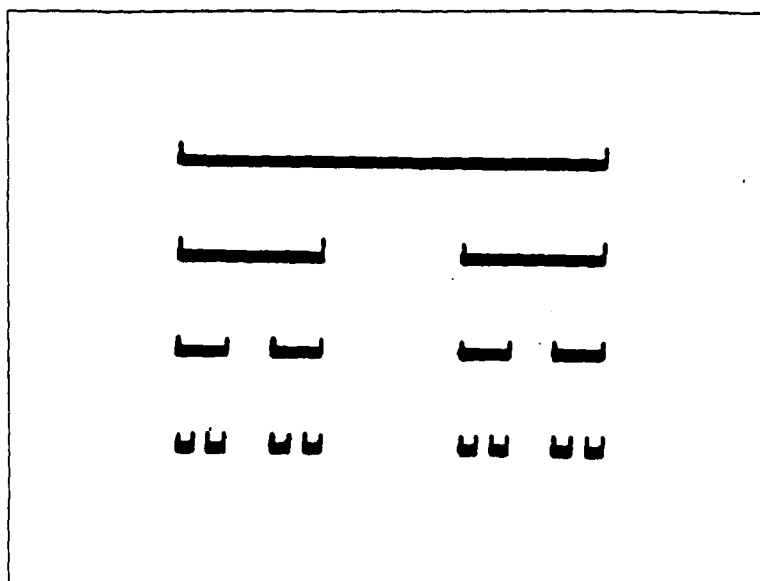
Figure 2.3. Triadic Cantor Dust [7:158]

extension of the box counting algorithm which is used for the fractal dimension estimations made in this thesis is explained in Chapter IV.

Still other methods, related to the statistics of the random variations of fractal shapes, have also been shown to be reasonably accurate measures of fractal dimension. These methods include the Grassberger-Procaccia Method [10:189], the Information Estimation Method [31:11], the Correlation Method [31:17], the Intensity Statistics Method [29:295], the Power Spectral Density Method [26:20], the Length of a Trail Method, the Area/Perimeter relationship, the Variance of Increments Method [5:38], and the Hybrid Brown Method [13:Chap 3-4]. Detailed explanations of those methods are not pertinent to this thesis and are not included here. For the reasons behind the choice of the estimation algorithm used in this thesis, the reader is referred to Chapter IV.

2.6 Summary

Fractal geometry is a new science which provides a mathematical and conceptual method for the study of shapes and objects that do not adhere to the principles of classical Euclidean geometry. Because these fractal shapes "look like" so many shapes that occur in nature they are useful in the modelling and segmenting of natural scenes. Fractals can

be described by a number, defined as the fractal dimension, which can be used to compare and contrast it with other fractals and Euclidean shapes.

Fractal geometry has already proven useful in the fields of cartography [27:1], land-form analysis [20:627], and computer graphics [8:35]. Even so, it seems the full potential for the use of fractals is yet to be fulfilled. Fractals show great promise in the areas of digital communications encoding [25:74], film making [36:26], and mass computer storage techniques [4:xi].

III. Synthetic Aperture Radar

3.1 Overview

This chapter describes polarimetric Synthetic Aperture Radar (SAR). It includes a brief description of the radar system used by JPL to collect the SAR data used in this thesis. It also defines the transmit and backscatter Stokes vectors and the target phase return matrix.

3.2 Synthetic Aperture Radar

Restating an earlier definition, SAR is an "airborne (or spaceborne) radar mapping technique for generating high resolution maps of surface areas and terrain." [37:185] Wehner states further that "the term synthetic aperture refers to the distance that the radar travels during the time that reflectivity data are collected from a point to be resolved on the earth's surface, which remains illuminated by the real antenna beam." [37:185] Because for real aperture radars the azimuth resolution is inversely proportional to the real antenna size, one way to improve the resolution (make it smaller) is by using a larger antenna [37:193]. By the use of a moving platform combined with clever processing, the real antenna size of the relatively small airborne radar antenna set can be synthetically expanded to improve the resolution of the radar. Specifically, an equivalently large aperture is synthesized by sequentially sampling the fields present at discrete points along the synthetic aperture length as the aircraft's small real aperture moves along the flight path. Thus the small real aperture is essentially "stretched" into a large synthetic aperture. The subsequent phase coherent summing of these values yields a return signal equivalent to the return signal which would have been collected from a large real aperture [19:20]. Thus SAR can provide an advantage of better azimuth resolution over radars employing only a similarly sized real aperture.

The resolution in the range direction is a product of conventional (real aperture) pulse duration measurement techniques which use transmitted pulses that are usually pulse compression waveforms. [24:443] [11:13].

3-1

3.3 Polarized Waves

Radar waves are polarized if their electric field is constrained in some fashion. If this E-field is constrained to one dimension, the polarization is linear [23:1]. Horizontal (H) and vertical (V) polarizations are common linear polarizations. Non-linear polarizations are called elliptical polarizations. Circularly polarized waves are a special case of the elliptically polarized waves. The ellipticity and orientation of an elliptically polarized wave are determined by the angular parameters χ and ψ, respectively. Figure 3.1 illustrates how χ and ψ determine the polarization of a radar wave.
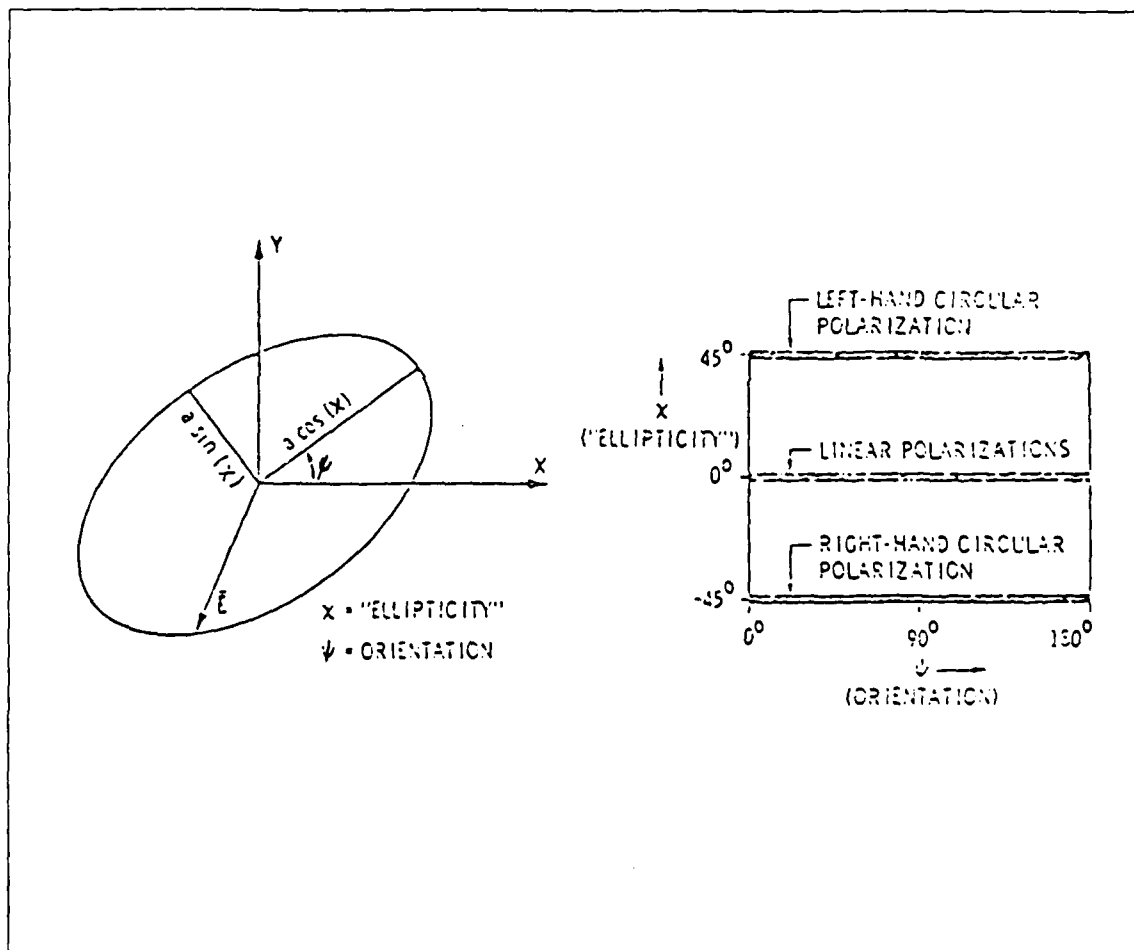
Figure 3.1. Ellipticity and Orientation of Waves [32:IV-1]

3.4 Transmit and Receive Configurations

Several combinations of transmit and receive polarization configurations are used in this thesis. The linear co-polarized configurations are designated as HH, for horizontally polarized transmit/horizontally polarized receive or VV for vertical transmit/vertical receive configurations. Similarly, HV designates the horizontal transmit/vertical receive cross-polarized configuration. Elliptically polarized transmitted waves are described by the parameters χ and ψ as explained above. The choices of values for χ and ψ necessary to generate the elliptically polarized transmitted waves that were used in this thesis were made in order to deviate from both strictly *linear* and strictly *circular* polarizations. In this manner, all of the elements of the target phase matrices would be exercised in the calculations of the Stokes vectors of the backscattered waves. (See Equation 3.6.)

3.5 Polarimetric SAR

A radar target can be considered as a polarization transformer [38:537]. This means the polarization properties of the transmitted wave are changed in some way by the target. These changes are a function of both the electrical and physical properties of the target. Therefore a good deal of information about the target is available in the polarization properties of the backscattered wave. Most conventional radar systems, however, do not take full advantage of all of the information available in this backscattered wave. They are usually limited in both transmit and receive polarization options [9:246] [34:529]. These systems also fail to retain any phase data when measuring and processing the backscattered waves for subsequent aid to image display [9:258] [34:529]. This thesis pursues the question of whether the use of either or both of these parameters, the polarimetric signature of a target, or the phase of the backscattered wave, can contribute to the target description, identification or segmentation processes.

3.6 JPL Equipment

Data used in this thesis was provided by the Jet Propulsion Laboratories. JPL used a modified conventional SAR system as an imaging radar polarimeter [34:529]. Equipment specifications for the JPL radar system can be found in Zebker et al.

The JPL radar set used two orthogonal linearly polarized antennas to transmit pulses which were alternately horizontally, then vertically polarized. The co-polarized and cross-polarized magnitude and phase return data was collected and used to synthesize the complete complex polarization signature of the targets [39:683] [34:529]. This information about the target is contained in its phase matrix.

3.7 Phase Matrix and Stokes Vectors

The phase matrix is a 4x4 element matrix which completely describes the polarimetric reflectivity properties of a target [32:A-2]. A Stokes vector is a 4x1 element matrix that represents the polarimetric properties of an electromagnetic wave. For a mathematical derivation of these matrices the reader is referred to Hurst, page 41 and Thompson et al, pages A-2 through A-10. The results of these derivations along with the JPL data collection and calculation techniques are stated here.

The four elements of the normalized transmitted stokes vector, $\overline{S_{TX}}$, can be computed from the ellipticity and orientation parameters as follows [32:III-6] :

$$
\begin{aligned}
t_{xx} &= 1 \\
t_{xy} &= \cos(\psi^2)\cos(\chi^2) \\
t_{yx} &= \sin(\psi^2)\cos(\chi^2) \\
t_{yy} &= \sin(\chi^2)
\end{aligned}
\tag{3.1}
$$

where

$$
\overline{S_{TX}} = \begin{bmatrix} t_{xx} \\ t_{xy} \\ t_{yx} \\ t_{yy} \end{bmatrix}
\tag{3.2}
$$

The backscattered waves were coherently collected by the JPL radar set. This data was used to determine the Stokes vector of the measured backscattered wave. The co-polarized and cross-polarized elements, b_{xx}, b_{xy}, b_{yx} and b_{yy}, compose the Stokes vector of the

backscattered wave, $\overline{S_{BS}}$. Where:

$$\overline{S_{BS}} = \begin{bmatrix} b_{xx} \\ b_{xy} \\ b_{yx} \\ b_{yy} \end{bmatrix} \qquad (3.3)$$

This data was then used to determine the 4x4 phase matrix of the target. Reciprocity is assumed so the phase matrix is symmetric. The elements of $\overline{P}$ are [32:A-3]:

$$
\begin{aligned}
P_{11} &= .25(I_{xxxx} + 2I_{xyxy} + I_{yyyy}) \\
P_{12} &= .25(I_{xxxx} - I_{yyyy}) \\
P_{13} &= .5Re(I_{xxxy} + I_{xyyy}) \\
P_{14} &= .5Im(-I_{xxxy} - I_{xyyy}) \\
P_{22} &= .25(I_{xxxx} - 2I_{xyxy} + I_{yyyy}) \\
P_{23} &= .5Re(I_{xxxy} - I_{xyyy}) \\
P_{24} &= .5Im(-I_{xxxy} + I_{xyyy}) \\
P_{33} &= .5Re(I_{xxyy} + I_{xyxy}) \\
P_{34} &= .5Im(-I_{xxyy}) \\
P_{44} &= .5Re(-I_{xxyy} + I_{xyxy})
\end{aligned}
\qquad (3.4)
$$

where

$$
\begin{aligned}
I_{xxxx} &= b_{xx}b_{xx}^* \\
I_{xxxy} &= b_{xx}b_{xy}^* \\
I_{xxyy} &= b_{xx}b_{yy}^* \\
I_{xyyy} &= b_{xy}b_{yy}^* \\
I_{xyxy} &= b_{xy}b_{xy}^* \\
I_{yyyy} &= b_{yy}b_{yy}^*
\end{aligned}
\qquad (3.5)
$$

The * in these equations denotes complex conjugation.

Once the phase matrix for a target was known, the Stokes vector of a synthesized backscattered wave could be calculated for any given transmit polarization by using the transmitted wave Stokes vector and the target phase matrix [32:A-2] [12:43]. Such that

$$\overline{S_{BS}} = \overline{P}\,\overline{S_{TX}} \qquad (3.6)$$

where

$$\overline{S_{BS}} = \text{4x1 Stokes vector of the backscattered wave}$$

$$\overline{P} = \text{the 4x4 matrix representing the scattering}$$
$$\text{parameters of a target}$$

$$\overline{S_{TX}} = \text{4x1 Stokes vector of the transmitted wave}$$

The four elements of the Stokes vector of the backscattered wave (as defined by Equation 3.3) were then used to calculate the magnitude and relative phase of the horizontally and vertically polarized components of the backscattered wave. The four elements of the Stokes vector are expressed in terms of the magnitudes and phase in Equation 4.1.

3.8   Summary

SAR provides a way to increase system resolution over that of a conventional real aperture imaging system. It also provides a method of collecting a great deal of data about a target via the complex components and polarimetric properties of the backscattered waves.

IV. Methodology

4.1 Overview

This chapter describes the methodology for this thesis. It includes the entire process of creating and displaying the image data, estimating the fractal dimensions of the different regions within the images, displaying the segmented regions and displaying the histograms which reveal the distribution of fractal dimensions estimated for each image.

4.2 Segmentation Process

One of the purposes of this thesis was to determine if areas or objects of interest in an SAR image could be segmented from other areas or objects in the same image by use of fractal geometry. To determine this, each 512x512 pixel dataset, representing an image scene, was divided into 4096 adjacent, non-overlapping regions of 8x8 pixels each. The fractal dimension of each of these 4096 regions was then estimated using an extension of the box counting algorithm. The frequency of occurrence of small intervals of these fractal dimensions were then plotted in a histogram. The segmented images were then displayed along side of the original image (with an 8x8 pixel grid overlay) to visually determine the effectiveness of the fractal geometry segmentation.

Figure 4.1 charts the methodology of this segmentation process. Each step of the methodology, data decompression and normalization, image display, fractal dimension estimation, generation of the histograms and image segmentation, is charted from the top down. The optional step of generating a three dimensional plot of the image "surface" is also shown.

Each of these steps was performed by FORTRAN programs written by the author for the Vax/VMS system. The names of these programs are enclosed in the boxes in Figure 4.1. Explanations of each are provided below and in the thesis supplement.

The SAR data that was obtained from JPL in a compressed format, was decompressed and normalized on a Digital Equipment Corporation (DEC) MicroVax computer. The images, segmentations and histograms were displayed on a DEC Microvax Workstation.

4-1

4.2.1 Segmentation Display Options. The segmentations could be displayed as "full segmentation signatures" which mapped the entire histogram of fractal dimensions from D_f equal to 2.0 through D_f equal to the maximum for that image dataset. Another option was to display all regions within the image with an estimated fractal dimension that fell within some user specified interval of interest contrasted against all regions with estimated fractal dimensions not within that interval. This interval of interest was often found by observing the "peaks" and "valleys" in the histograms and choosing intervals based upon these observations.

4.3 Datasets

The second purpose of this thesis was to determine if the polarimetric complex valued data (the magnitude and phase) of the SAR returns yield any additional information about the target scene than the power return values used in conventional SAR analysis. In pursuit of this answer, segmentations for each scene were accomplished using nine different image datasets. These nine datasets all included an X and Y coordinate corresponding to the ground location of a pixel, but varied in the other parameter(s) chosen to encapsulate information contained in the SAR returns. These nine datasets contained:

1. HH co-polarized power returns

2. VV co-polarized power returns

3. HV cross-polarized power returns

   - Reciprocity was assumed therefore the VH power returns were identical to the HV power returns [21:150].

4. Both the HH and VV power returns. This dataset was designated POL.

5. All three power returns, HH, VV and HV. This dataset was designated 3POL.

6. δ, the phase returns from an elliptically polarized transmitted wave.

7. A_H, the horizontally polarized magnitude returns from an elliptically polarized transmitted wave.

Designation	Dataset Contents	Euclidean Dimension
HH	X, Y, HH power returns	3
VV	X, Y, VV power returns	3
HV	X, Y, HV power returns	3
POL	X, Y, HH, VV	4
3POL	X, Y, HH, VV, HV	5
δ	X, Y, δ phase returns	3
A_H	X, Y, Horiz magnitude returns	3
A_V	X, Y, Vert magnitude returns	3
FULL	X, Y, δ, A_H, A_V	5

Table 4.1. Summary of Available Datasets

8. A_V, the vertically polarized magnitude returns from an elliptically polarized transmitted wave.

9. All three complex values, δ, A_H, and A_V from an elliptically polarized transmitted wave. This dataset was designated FULL.

These different datasets represented "surfaces" of varied Euclidean dimension. This is illustrated in Table 4.1. Datasets of HH, VV, HV, δ, A_H, and A_V represent three dimensional Euclidean surfaces (including the X and Y components). Dataset POL represents a four dimensional Euclidean surface. FULL and 3POL represent five dimensional Euclidean surfaces. The Euclidean dimension of these datasets relate directly to the number of degrees of freedom of the data that comprise each set.

4.4 Implementation

4.4.1 Creating Images. The SAR data for each of the scenes used in this thesis was provided by JPL. All of the polarimetric data for the scenes was stored in a compressed format on magnetic tape readable by a VAX machine using the VMS operating system. Complete step-by-step instructions of how the compressed data files were copied from magnetic tape to the VAX disk can be found in the supplement to this thesis.

4.4.2 Data Decompression. After the data files were copied to the VAX disk, they had to be decompressed. This was accomplished by using a modified version of a JPL software program called Multitest. This program was available on one of the magnetic tapes along with data from one of the scenes provided by JPL. Instructions for copying this program to the VAX disk are included in the supplement.

The program Multitest decompresses the data for a given transmit and receive polarization (as specified by the user) and outputs a power return for each pixel in the image. To create all nine datasets it was necessary to modify Multitest to output both the power values for each pixel along with the complex data δ, A_H, and A_V. The Multitest program was further modified to change the size of the output decompressed data file to a 512x512 pixel image. This image size was chosen because of its convenience for display on the MicroVax workstation.

4.4.3 Creating Datasets. The nine different datasets were created by using two different modified versions of Multitest. One version created datasets for the power images, the other for complex (magnitude and phase) images.

4.4.3.1 Power Images. Data for images which show the power returns for each of the pixels in the 512x512 pixel images were obtained by using the program DECOM. This program was created by modifying Multitest to output the 512x512 pixel decompressed power return datasets. After DECOM calculated the power return data for each of the desired transmit and receive polarizations, the real valued numbers in these datasets were normalized to integer values in the range 1 through 255 which mapped to an 8-bit color map for subsequent image display.

The normalization program used for all power return datasets was called NNORM. This program linearly mapped all of the real valued power returns in the decompressed datasets between 0.001 and 1.0 to integer valued numbers between 1 and 255. The overall mapping process however was non-linear from the minimum value to the maximum value within the computed power datasets. The values between 0.001 and 1.0, which represented the extreme low scale of the dataset values, were emphasized over values outside this range

because values within this range were very common and those outside this range were rare. Enhancing these low values was equivalent to applying a constant amplification to the returns which brightened and enhanced the images. This normalization process provided a very recognizable image. Other attempted linear methods of normalization did not create recognizable images.

4.4.3.2 Complex Images. The JPL program Multitest was modified to produce datasets representing a 512x512 pixel image where each pixel was represented by δ, A_H and A_V. These real number values which represent the complex valued returns were calculated using the information contained in the Stokes vectors of the backscattered waves.

The calculations to determine both the Stokes vector of the transmitted wave (for any user specified polarization), the phase matrix, and the values δ, A_H, and A_V for each of the pixels in the scene were done by the program COMPLEX.

COMPLEX was a modified version of Multitest which suppressed the calculation and output of the power return values for each pixel but calculated and passed both the transmitted wave Stokes vector and the phase matrix for each pixel to the subprogram BACK. BACK used Equation 4.1 to solve for, calculate and output the three values δ, A_H and A_V corresponding to each of the 512x512 pixels in the image.

The 4x1 Stokes vector of the backscattered wave was broken down into its four elements b_{xx}, b_{xy}, b_{yx}, and b_{yy}, where each of these components was described by [32:A-2]:

$$
\begin{aligned}
b_{xx} &= A_H^2 + A_V^2 \\
b_{xy} &= A_H^2 - A_V^2 \\
b_{yx} &= 2 A_H A_V \cos(\delta) \\
b_{yy} &= 2 A_H A_V \sin(\delta)
\end{aligned}
\tag{4.1}
$$

where A_H, A_V and δ are as previously defined.

These real valued datasets were then normalized to integer values between 1 and 255 which were mapped to an 8-bit color map for subsequent image display. This process was

accomplished by the program COMPNORM. The normalization of A_H and A_V values was similar to the normalization process for the power return datasets described above. The δ values however, were linearly mapped from the minimum through the maximum observed values to integers between 1 and 255, as this method provided the most recognizable images.

4.5   Displaying Images

Images were displayed in one of two ways. The program IMAGE created images using a color map ranging from dark blue for low valued integers (approaching 1), through green for intermediate values, to dark red for the highest values (approaching 255) in the normalized datasets. The program GRID8 performed the same function as IMAGE but also overlayed a grid of 8x8 pixel boxes over the image. This grid was useful in comparisons between actual image data and the segmentations of these images.

4.6   Fractal Geometry Segmentation Process

Program listings and descriptions of the functions of the FORTRAN programs that performed the fractal dimension estimations, the segmentation displays and the histogram displays are included in the supplement to this thesis.

4.6.1   Estimating Fractal Dimensions.
The first step in segmenting SAR images using fractal geometry was to determine the distribution of the estimated fractal dimensions for each of the 4096 8x8 pixel regions in a given image. This was done by applying an extension of the box counting algorithm [4:176] [35:56]. An extension of the published algorithm was necessary to facilitate estimations of fractal dimensions exceeding 2.0. This was necessary because estimations were made on image "surfaces" which varied in Euclidean dimension from 2 through 5.

4.6.1.1   Choice of Algorithm.
The extended box counting algorithm was chosen to perform the fractal dimension estimations because of its seeming ease of comprehension and computer implementation. Much of the more recent literature [2:1661] [33:1390]

[31:13], published after this decision was made, state the impracticalities or inefficiencies of the box counting algorithm for "high" imbedded dimensions. However only one author defines the difference between high and low dimensions. Simm et al define low fractal dimensions such that $D_f < 2.0$ and high dimensions such that $D_f > 2.0$ [28:518]. By this definition, all of the estimates made in this thesis were high dimensions. However, considering that the fractal dimensions of some strange attractors (a set which describes the behavior of a dissipative dynamical system - usually represented by a nonlinear differential equation [28:511]) about which most of the recent literature is concerned, have been estimated at above 15.0 [1], any estimate of D_f less than five was relatively low. Further, since this thesis was the exploration of a new method, and it was desired only to get an indication of the worth or "proof of concept" of this method, some minor inaccuracies in the estimations made here were acceptable. In any event, the effect of any such errors tended to be cancelled by the effects of the comparisons made between estimated fractal dimensions of different image regions which were part of the segmentation process.

4.7 Description of the Extended Box Counting Algorithm

A fractal dimension was estimated for each of the 4096 regions of an image. These regions were defined by an 8x8 pixel base in the X and Y coordinates. Data for a third dimension was read from the specified dataset and normalized to values between 1 and 8. This normalization was required so that the dataset representing the "surface" would be bounded by a cube of side length 8. Thus the maximum deviation in any Euclidean dimension (including the X and Y dimensions which were chosen to be bounded by an 8x8 pixel region) within the dataset would be 8 units. If applicable for the dataset under observation, this normalization process was also performed on the data representing the fourth and fifth Euclidean dimensions. Each 8x8 pixel region was then divided into adjacent and non-overlapping cubes (or hypercubes for datasets of Euclidean dimension 4 or 5) of a given side length. A count of the number of these cubes necessary to cover each of the values defined by the dataset values in all Euclidean dimensions was performed. This cube count was duplicated for cube sizes of side lengths 2 pixels and 4 pixels. The fractal dimension of each region was estimated using Equation 2.1 for cube sizes of both 2 pixels

and 4 pixels. An average of these two independent estimations was taken as the final estimated fractal dimension for that region.

4.7.1 Why an Average. An average of the two estimations instead of the more common (and mathematically rigorous) use of a limit as cube size approaches zero was used for two reasons. First, the average was a much easier value to compute. Second, the limit as cube size approaches zero (See Equation 2.2) takes on an indeterminate form for quantized data (See Section 4.8) and must be obtained by L'Hospital's rule [15:31] or by measuring the slope of a line of best fit on a log/log plot of the number of cubes counted versus the cube size [35:26].

The process of averaging the two independent estimates was thought to introduce no more error in the final estimation than would have attempting to find this line of best fit for these curves. To test this point, the slope of a log/log plot was calculated and fractal dimensions estimated for several regions picked at random. The averaging method and the slope of the line of best fit method gave similar results for these regions. This comparison is summarized in Table 4.2.
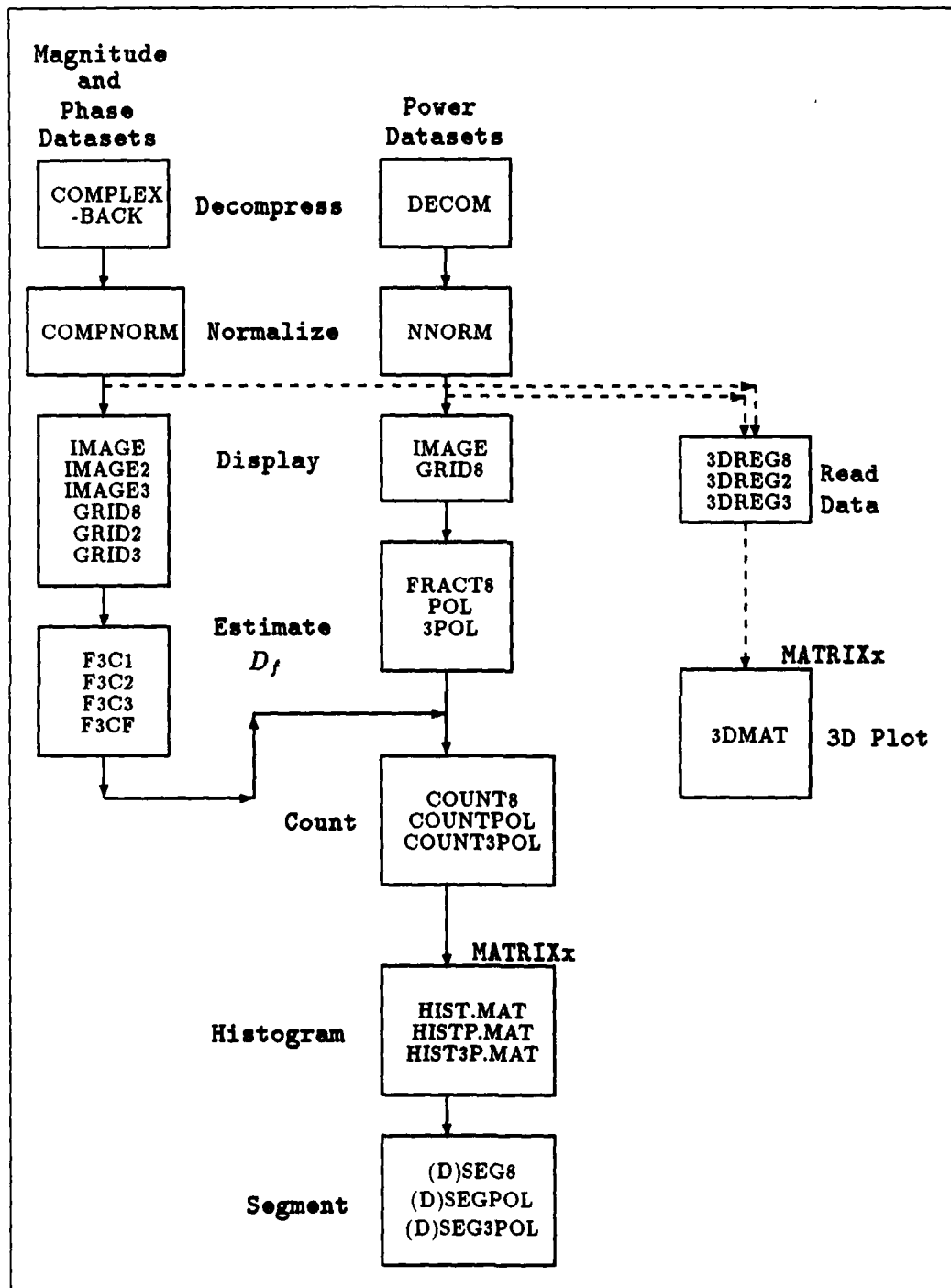
Figure 4.1. Flow Chart of Methodology

Region #	# of cubes		ln(# of cubes)		Δy	Δx	m	D_f		Ave D_f	% error
	size=2	size=4	size=2	size=4				size=2	size=4		
1	61	8	4.1	2.1	2.0	.693	2.89	2.97	3.00	2.98	3.11
2	37	6	3.6	1.8	1.8	.693	2.60	2.60	2.58	2.59	0.40
3	16	4	2.8	1.4	1.4	.693	2.02	2.00	2.00	2.00	1.00
4	24	5	3.2	1.6	1.6	.693	2.30	2.29	2.32	2.31	0.40
5	51	7	3.9	1.9	2.0	.693	2.89	2.83	2.81	2.82	2.42
										Ave error	1.47%

Table 4.2. Comparison of Average Fractal Dimension and Slope Approximation

Table 4.2 compares the averaging method to the slope of the line of best fit method for five regions selected at random. The table values have been rounded off for ease of display. The number of cubes counted for cube sizes of both 2 pixels and 4 pixels are shown. Data was provided from the cube counting process which was part of the fractal dimension estimation procedure. If these two datapoints were plotted on a log/log plot, as explained above, the approximate slope of the line of best fit would be given by Equation 4.2. Since only two datapoints were available for each plot, the line of best fit was merely a line with endpoints at the datapoints.

$$m = \frac{\Delta y}{\Delta x} = D'_f \tag{4.2}$$

where

m = the slope of the line

D'_f = the fractal dimension estimate by line of best fit method (4.3)

Δy = ln(# of cubes of size=2) − ln(# of cubes of size=4)

Δx = ln(4) − ln(2) = .693

The two estimates of D_f, for cube sizes of 2 and 4 pixels, were calculated using Equation 2.1. The average of these two estimates was compared to D'_f. The greatest "error" between the two different methods of estimating the fractal dimension of the regions

was 3.11%. The average "error" was approximately 1.47%. The two methods clearly give almost identical results.

4.7.2   Choice of Region Size.   The use of regions of base size 8x8 pixels was determined by trying several different sizes and using the one that provided the best compromise between conflicting requirements. On one hand, it was desired to keep the region size as small as possible, which meant "good resolution" of the segmented regions. This was in conflict however, with a desire to have the regions remain large enough such that as many different cube sizes (less than the 8x8 pixel region size) as possible could be used in the fractal dimension estimation process, thus increasing the accuracy of these estimates.

Regions of size 32x32 pixels and 16x16 pixels were tried and rejected as too large to display any details of the image in the segmentations. A region size of 4x4 pixels was rejected because it was so small that it allowed fractal dimension estimations using only one cube size, that of side length equal to 2 pixels. Use of only this one estimation may have introduced unacceptable errors. Many authors [22:671] [29:295] [5:40] [31:16] [30:4460], discuss this problem of choosing the proper region size without a clear answer.

4.8   Quantized Surfaces

It should be noted that each of these "surfaces" represented by the datasets was actually a "quantized surface." Since data was available only for each pixel and the pixels were some finite distance apart (representing the resolution of the radar) the "surfaces" were not continuous. No attempt was made to interpolate values between observed pixel values for any of the fractal dimension estimations. This was not thought to have contributed any significant error or bias to the estimation process. However, even if it had done so, this error would have been similarly biased for each of the regions for which a fractal dimension is estimated, and would not have hampered any segmentation based upon comparisons between these estimations. A quantification and study of the impact of possible errors of this type is left for the future.

4.9 Examples of Fractal Surfaces

Figures 4.2 through 4.4 show examples of the "surfaces" represented by one of the three dimensional (Euclidean) datasets. The estimated fractal dimension of each region is given under the respective figures. The fractal dimensions of the surfaces increase with their apparent "roughness." The MATRIXx software package used to generate these figures shows connections between the individual pixel values in the 8x8 pixel regions shown. As explained above, this type of interpolation was not done by the fractal dimension estimation algorithms.
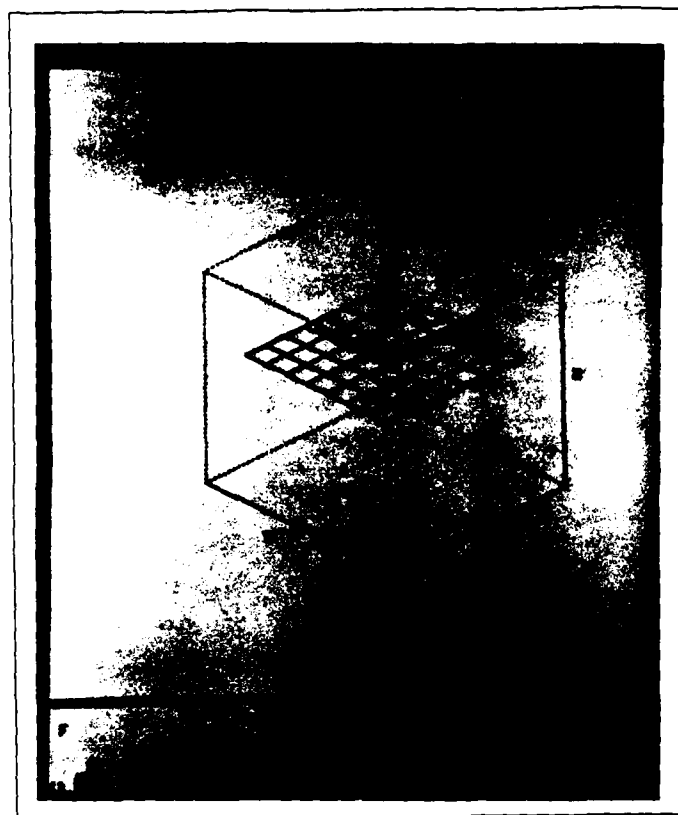
Figure 4.2. 3-D plot of surface with $D_f = 2.00$

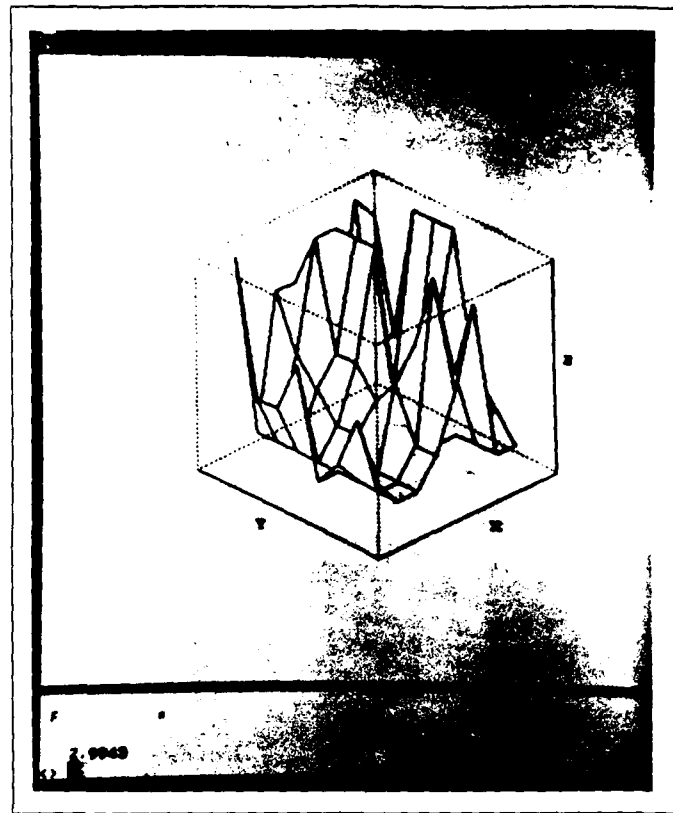Figure 4.3. 3-D plot of surface with $D_f = 2.4633$

Figure 4.4. 3-D plot of surface with $D_f = 2.9943$

4.10 Generation of Histograms

After the fractal dimension of each of the 4096 regions was estimated, a histogram was plotted charting the number of occurrences of fractal dimension within a series of small intervals spanning the range from the minimum estimated fractal dimension to the maximum estimated fractal dimension for that dataset. The width of the intervals (bars of the histograms) was arbitrarily chosen to be 0.04. This was a reasonable number because it created a very readable histogram and simultaneously represented a small enough interval to differentiate between similiar estimates of fractal dimension. The software package MATRIXx was used to plot these histograms. Details on the use of MATRIXx are included in the supplement to this thesis. "Peaks" and "valleys" in these histograms separated the groupings of estimated fractal dimensions of the regions within a dataset. These groupings of fractal dimensions were used to help generate the segmentations of the datasets.

4.11 Displaying Segmentations

Two different options were used to display the segmented images. The "full segmentation signature" displayed all of the estimated fractal dimensions for a dataset in one image. In these segmentations, the low fractal dimensions (approaching 2.0) were mapped to dark blue, intermediate values to green and the highest estimated values (approaching the degrees of freedom for that dataset) to dark red. The full segmentation signatures gave an indication of the spatial relationships between regions of similar or different fractal dimensions. These signatures were often very useful in determining the utility of the fractal dimension segmentation process.

The second method of displaying segmented images was useful when working with the histograms. Regions with estimated fractal dimensions within a user specified interval were displayed as dark red against a blue background. The blue background represented those regions with estimated fractal dimensions outside of the specified interval. This type of segmentation display was useful when a high contrast segmentation display was desired.

4.12 Summary

The SAR data from the JPL magnetic tapes was decompressed. The data of interest (either the power return values or the magnitude and phase values) was calculated and arranged into nine different datasets. These datasets were then normalized to integer values between 1 and 255. They were then ready for display as images of the particular scenes or to be run through the fractal dimension estimation algorithms. After the fractal dimensions of the regions within the datasets had been estimated, histograms were produced illustrating the distribution of the estimated dimensions. The segmentations were then ready for display as either the full segmentation signature or as contrast segmentations highlighting only those regions within the scene that had estimated fractal dimensions within a user specified interval.

V. Results

5.1 Overview

This chapter presents the results of this thesis. It includes descriptions and images of each of the scenes used in the analysis of the segmentation process. It describes the analysis processes in which these segmentations were judged by both subjective and objective standards.

5.2 Description of Scenes

The segmentation process was performed on three scenes.

- One scene was a view of the San Francisco, California area. The scene included the Golden Gate Bridge, the city area with interior parks, the San Francisco Bay, and a natural region of rough terrain north of the bridge.

- The second scene was a different view of the Golden Gate Bridge. It included the water, a portion of the bridge, some natural regions and a small portion of the city.

- The third scene was of Moffett Airfield. This scene included an airfield, a city with visible main roads, and a river surrounded by forested regions north of the city.

The pixel resolution of each of these scenes was approximately 10x10 meters.

5.3 Results

Two different examination procedures were used to determine the quality or effectiveness of the segmentations. One was a purely subjective analysis performed on various segmentations of the three scenes. The other method was an attempt to objectively quantify, by means of a figure of merit, the effectiveness of the segmentations in order to evaluate which datasets yielded the best segmentations. Explanations of these two analysis procedures and their results are presented below.

5.4 Subjective Analysis

The following figures represent the images, segmentations and histograms for several of the datasets created for each of the three scenes. Not all of the dataset segmentations are shown here. The following figures were chosen to illustrate general results.
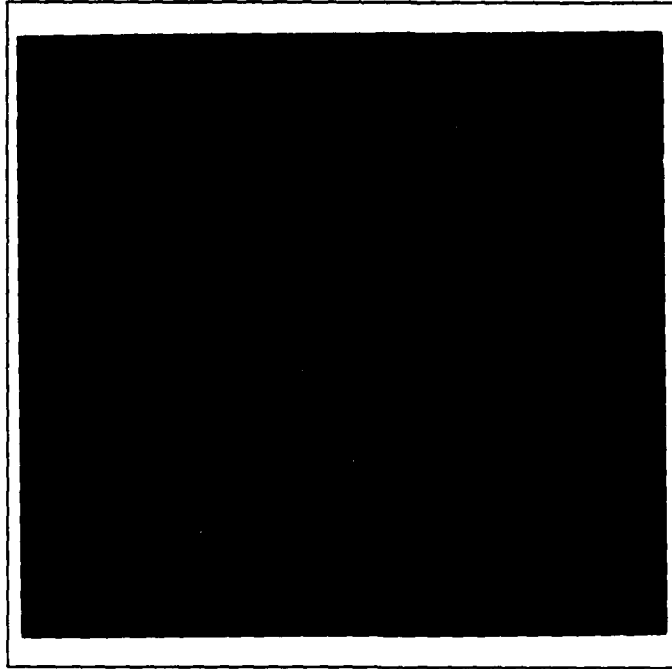
Figure 5.1. San Fran HH Image

Figure 5.1 is an image of the San Francisco scene showing the power returns from an HH co-polarized wave. The image clearly shows the city, parks, bridge and natural regions.
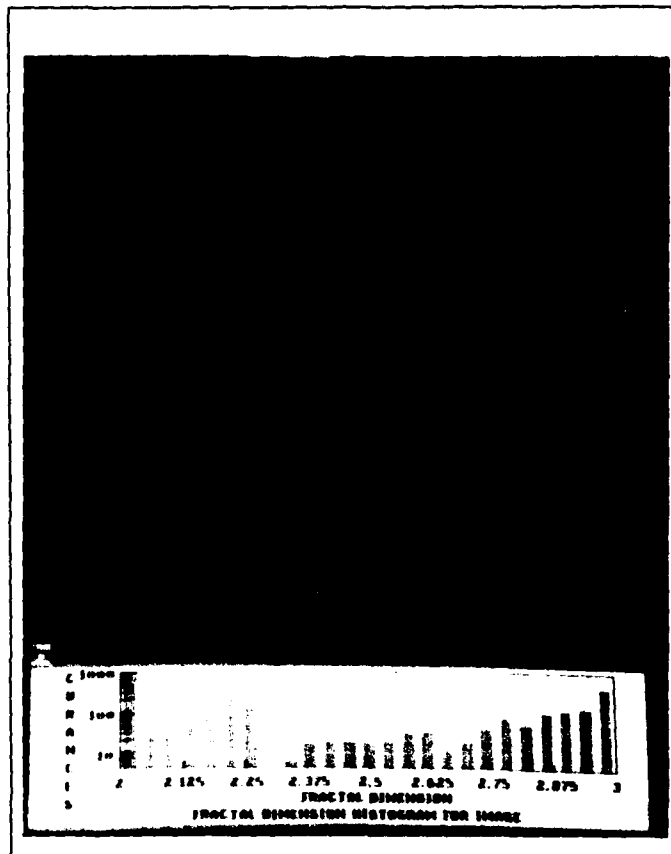
Figure 5.2. San Fran HH Full Segmentation Signature

Figure 5.2 is the full segmentation signature for the image in Figure 5.1 and the histogram for this segmentation. This figure shows that the fractal geometry segmentation was able to differentiate most of the major regions and some of the details of the image. The histogram shows a large number of regions with estimated fractal dimensions near 2.25. These regions are generally regions which determine the boundaries between the major areas or features in the image. The highest estimated fractal dimensions (approaching 3.0) are in those regions corresponding to the city and the rough natural terrain.
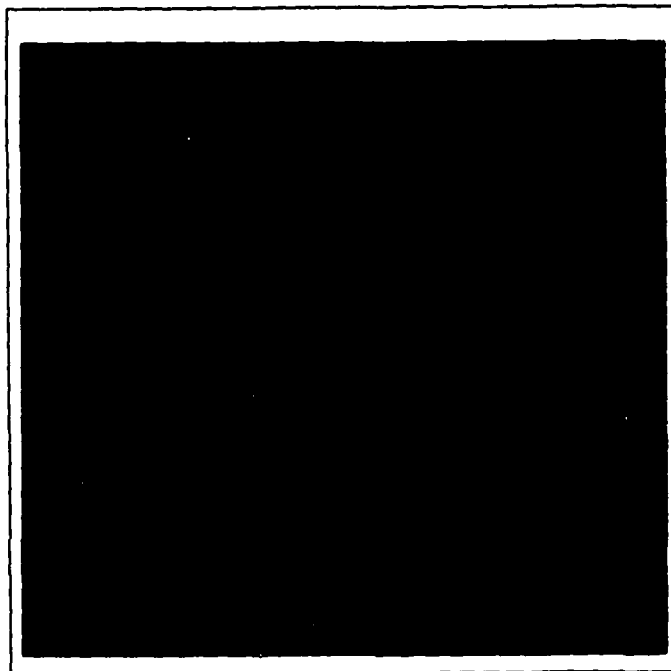
Figure 5.3. San Fran VV Image

Figure 5.3 shows the same scene generated from VV power return data. The VV power return image shows more roughness in the water than does the HH power return image. This is consistent with the literature concerning polarimetric power returns from sea clutter [9:252].
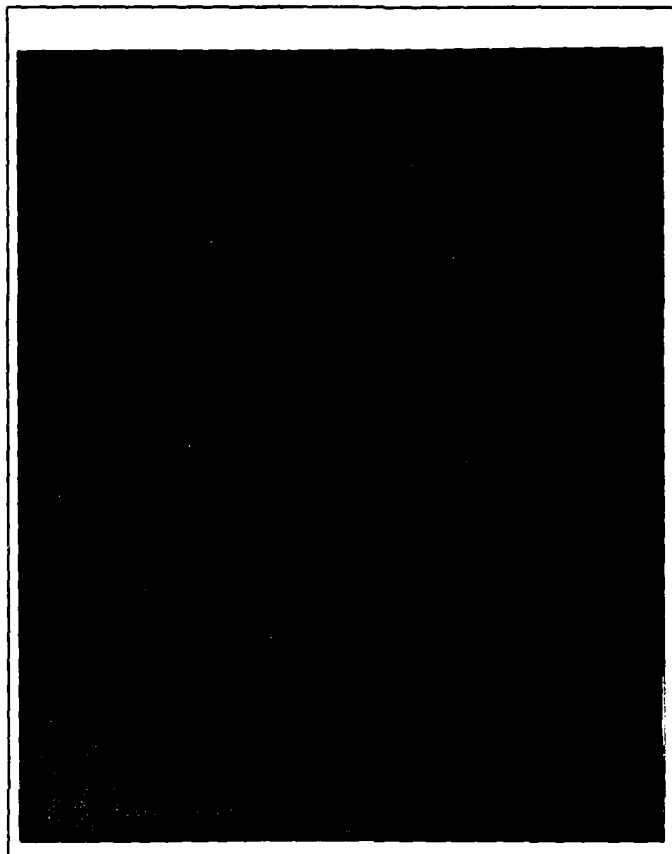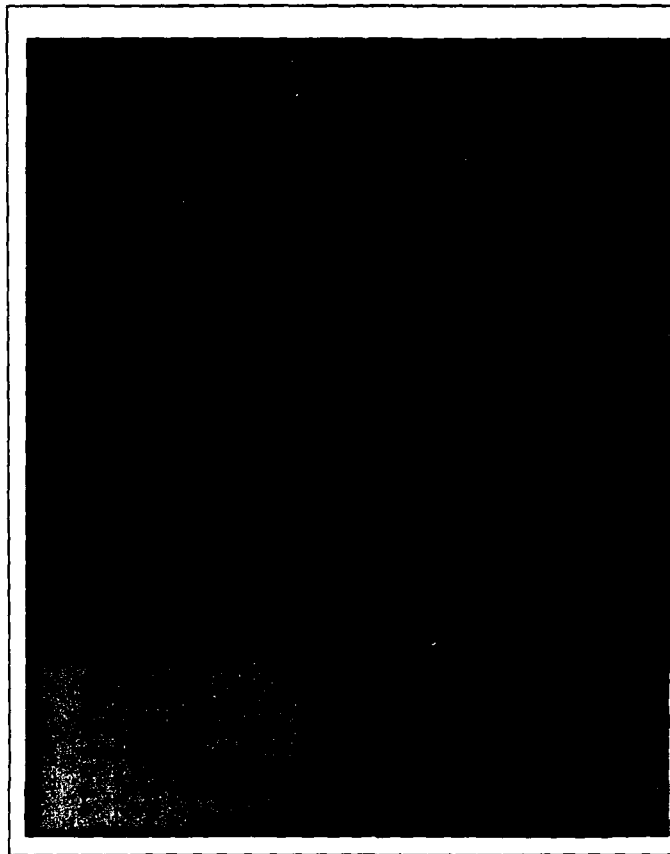
Figure 5.4. San Fran VV Segmentation, $2.75 \leq D_f \leq 3.0$

Figure 5.4 is the histogram and contrast segmentation for the image in Figure 5.3. The segmentation highlights those regions with estimated fractal dimension between 2.75 and 3.0. This segmentation does a reasonable job of separating the land from the water.

Figure 5.5. San Fran POL Segmentation, $3.75 \leq D_f \leq 4.0$

Figure 5.5 is the histogram and contrast segmentation for the 4 dimensional (Euclidean) dataset, POL, which includes the HH and VV power returns. The segmentation highlights those regions with an estimated fractal dimension between 3.75 and 4.0. This segmentation highlights the city regions.
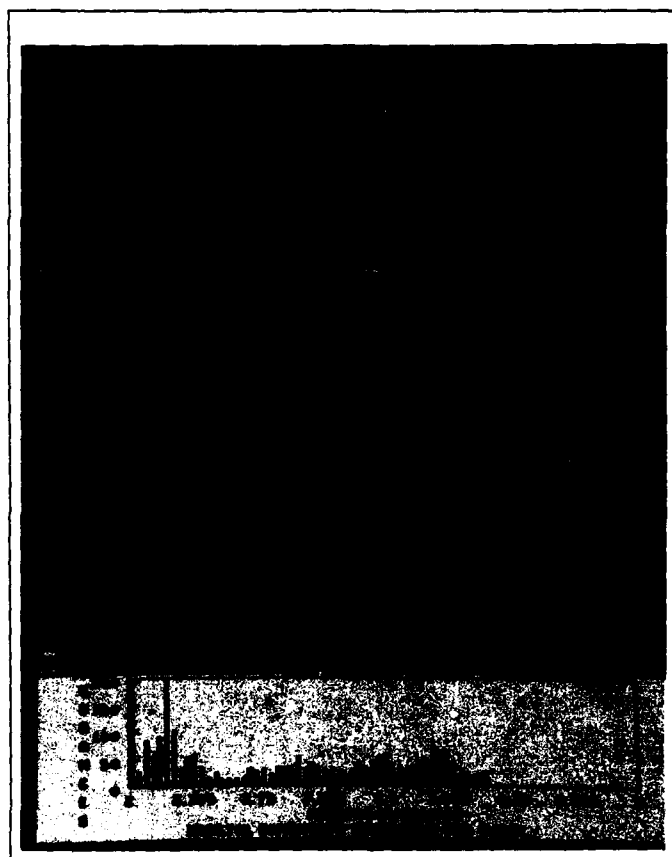
Figure 5.6. San Fran 3POL Segmentation, $3.75 \leq D_f \leq 5.0$

Figure 5.6 is the histogram and contrast segmentation of the 5 dimensional dataset, 3POL, which includes the HH, the VV and the HV power returns. The segmentation highlights those regions with estimated fractal dimensions between 3.75 and 5.0. This segmentation approximates a separation between manmade versus natural occurring areas in the scene.
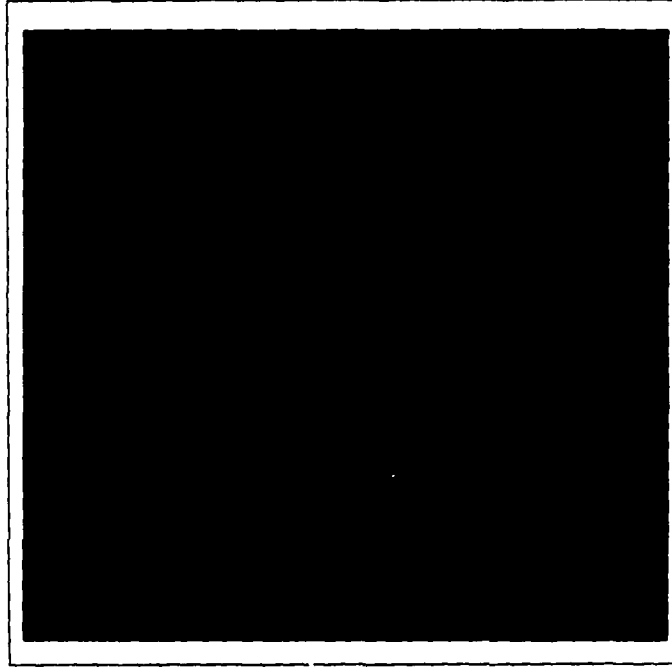
Figure 5.7. San Fran δ Image

Figure 5.7 is an image of the same scene generated using only the values of δ, the phases of the return waves. It is difficult to determine much detail about the scene from this image.
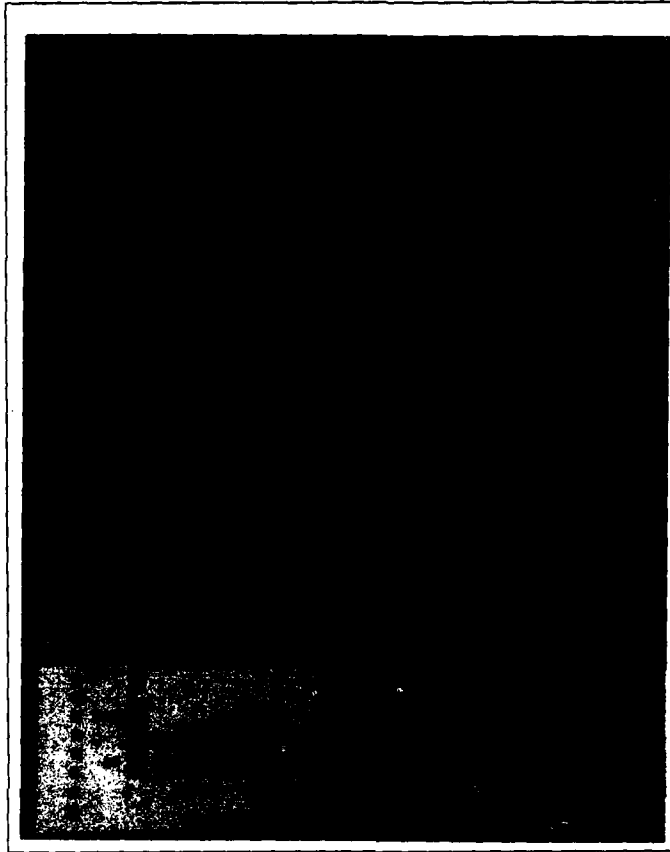
Figure 5.8. San Fran δ Full Segmentation Signature

Figure 5.8 is the full segmentation signature for the image in Figure 5.7. The segmentation actually shows more detail about the scene than does the image.
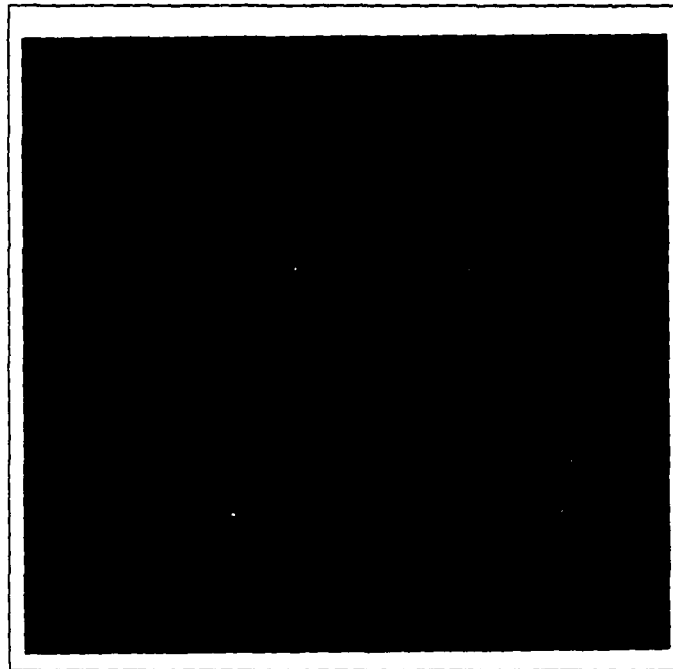
Figure 5.9. San Fran A_H Image

Figure 5.9 is the image generated from the dataset containing only A_H, the magnitude of the horizontally polarized component of an elliptically polarized transmitted wave with $\chi = -30$ and $\psi = 30$ degrees. This image shows great detail about the scene.
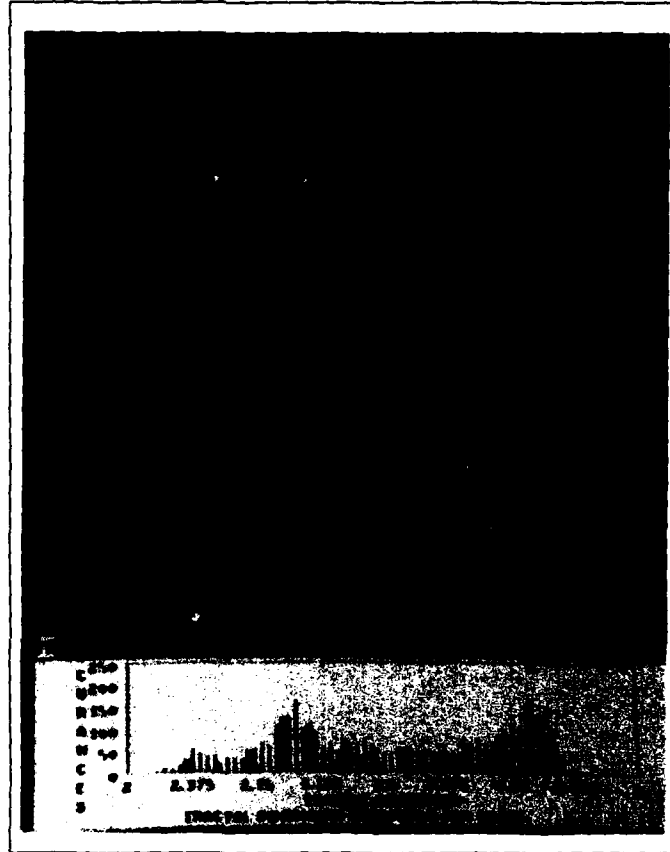
Figure 5.10. San Fran FULL Segmentation, $4.0 \leq D_f \leq 5.0$

Figure 5.10 is the contrast segmentation and histogram of the five dimensional dataset, FULL, containing δ, A_H and A_V values for the $\chi = -30$, $\psi = 30$ transmitted polarization. This segmentation highlights regions with estimated fractal dimension between 4.0 and 5.0. It provides a good separation between land and water.
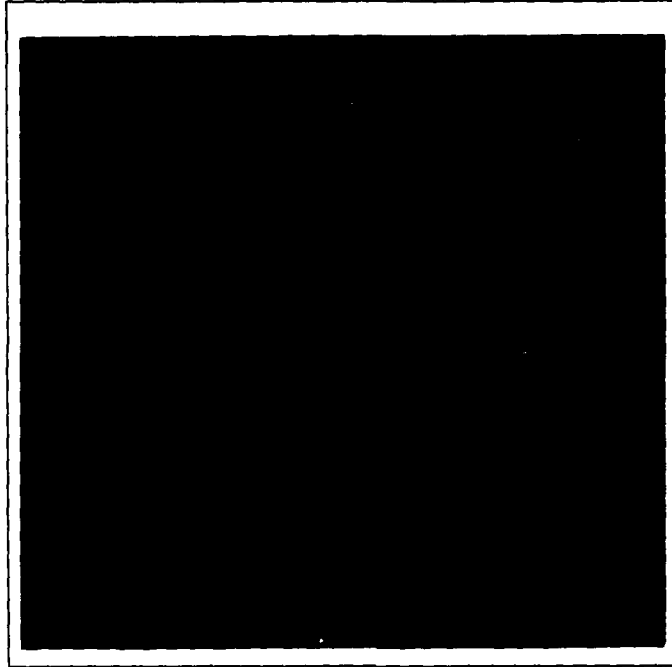
Figure 5.11. Moffett HH Image

Figure 5.11 shows an image of the scene of Moffett Field. The image was generated using values of HH power returns.
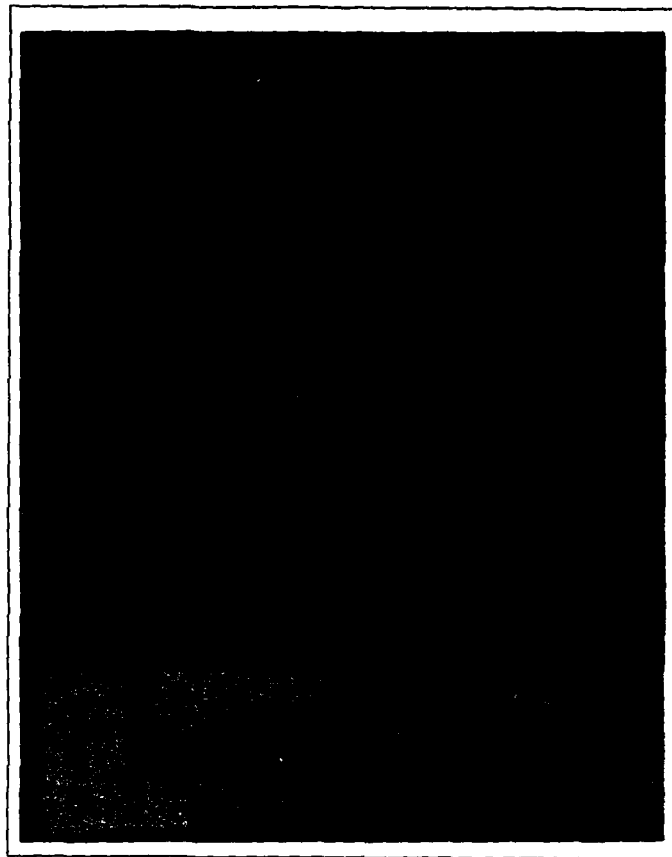
Figure 5.12. Moffett HH Full Segmentation Signature

Figure 5.12 is the full segmentation signature of the image in Figure 5.11. It shows some separation between the city and the airfield and plains to the north.
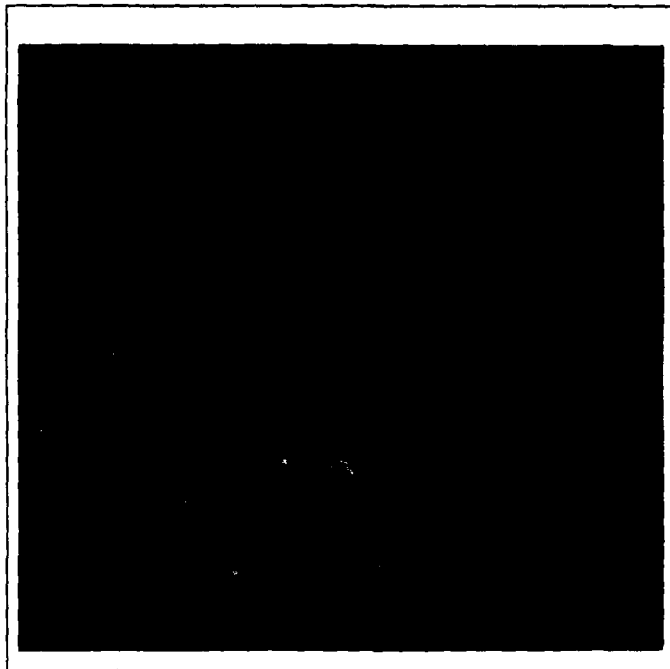
Figure 5.13. Moffett HV Image

Figure 5.13 is an image of the same scene generated using the HV power returns. It shows much less detail than do either of the HH or VV (not pictured for this scene) power return images. This may be due in part to non-optimal normalization of the HV power return dataset.
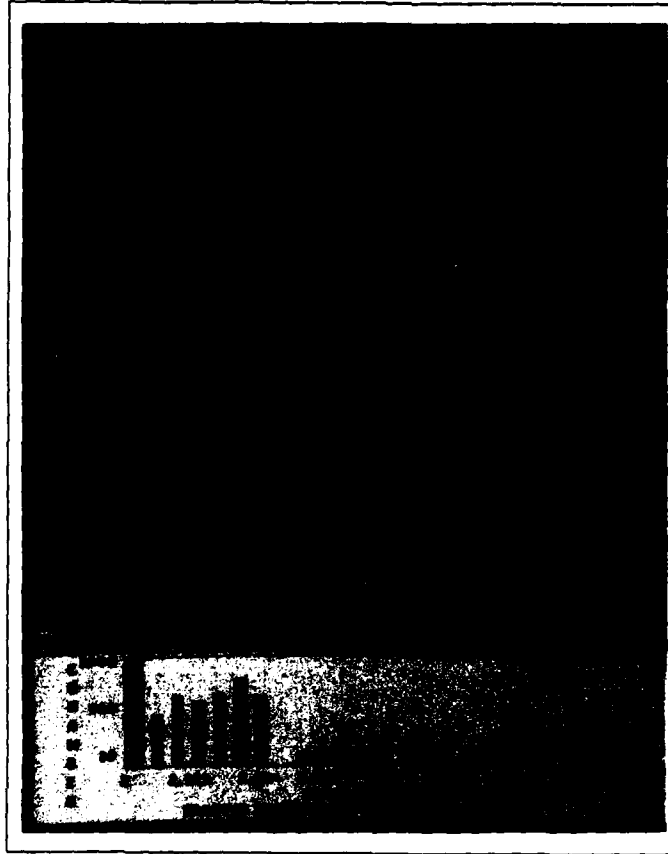
Figure 5.14. Moffett HV Segmentation, $2.05 \leq D_f \leq 3.0$

Figure 5.14 is the histogram and contrast segmentation of the HV power return dataset imaged in Figure 5.13. The segmentation highlights those regions with estimated fractal dimensions between 2.05 and 3.0. With the exception of the airfield, this segmentation separates the man-made areas from the natural areas in the scene.
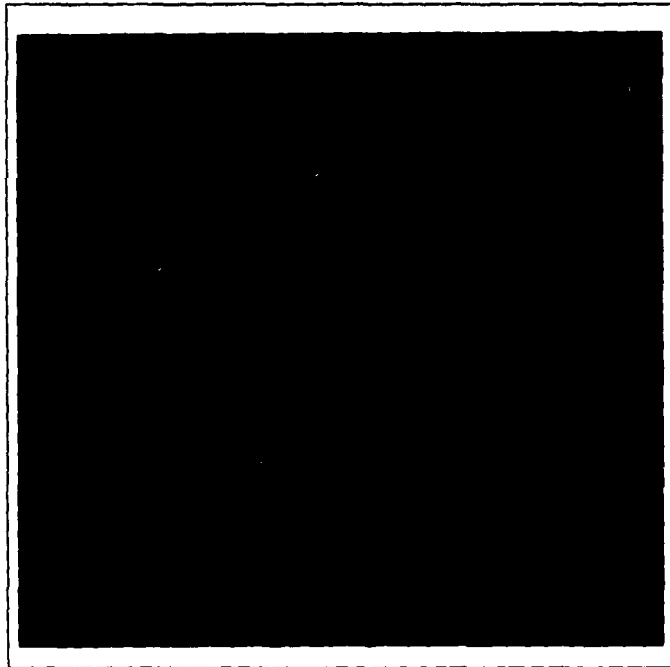
Figure 5.15. Moffett δ Image

Figure 5.15 is the image of the Moffett Field scene generated using δ, the phase returns, from an elliptically polarized transmitted wave with $\chi = 5$ and $\psi = -40$ degrees. As seen previously with the phase-only images, it is difficult to determine any details about the scene.
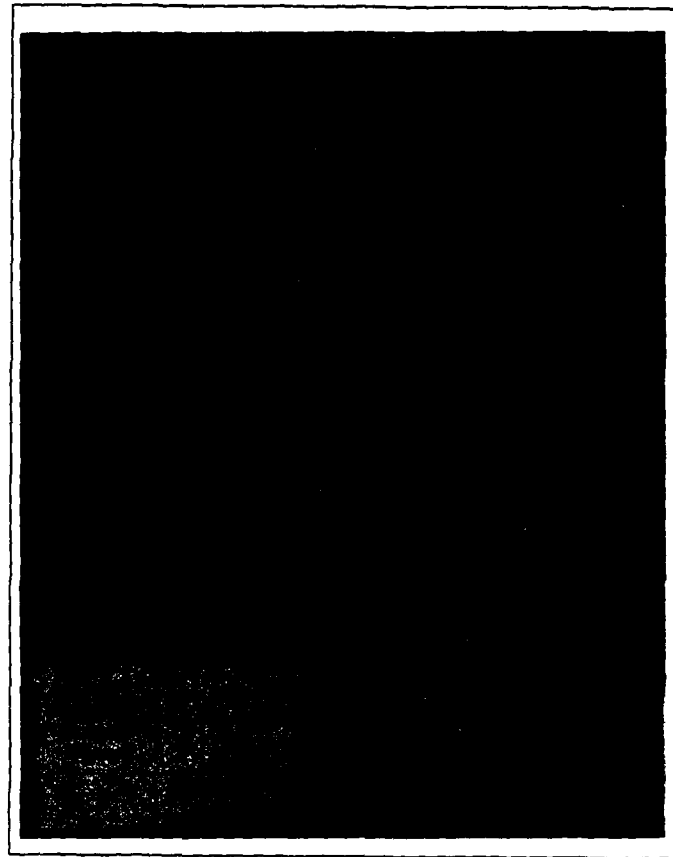
Figure 5.16. Moffett δ Segmentation, $2.8 \leq D_f \leq 3.0$

Figure 5.16 is the histogram and contrast segmentation of the image in Figure 5.15. The segmentation highlights those regions with estimated fractal dimensions between 2.8 and 3.0. This segmentation separates the man-made areas from the natural areas in the scene.
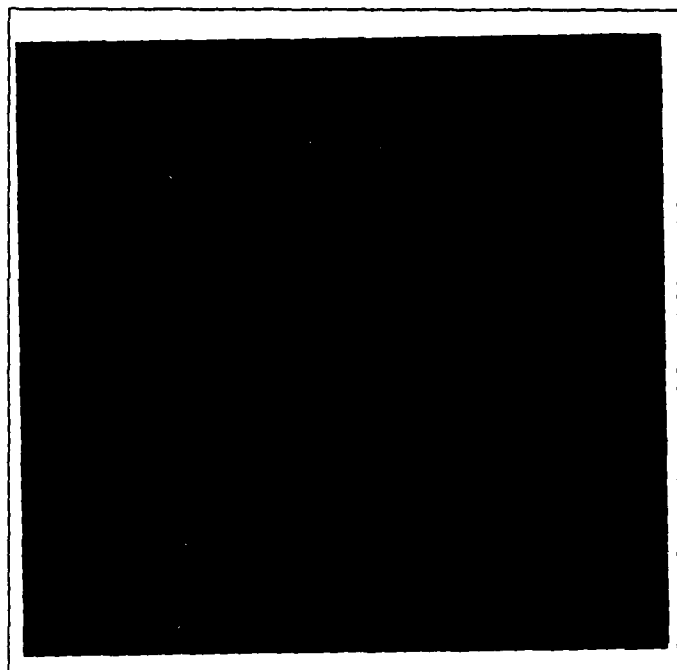
Figure 5.17. Moffett A_V Image

Figure 5.17 is the image generated using only the A_V magnitude returns from the $\chi = 5$, $\psi = -40$ degree elliptically polarized transmitted wave. While this is generally quite a good image of the scene, there is some vertical "smearing" in the forested areas north of the city. The cause of this smearing is not known.
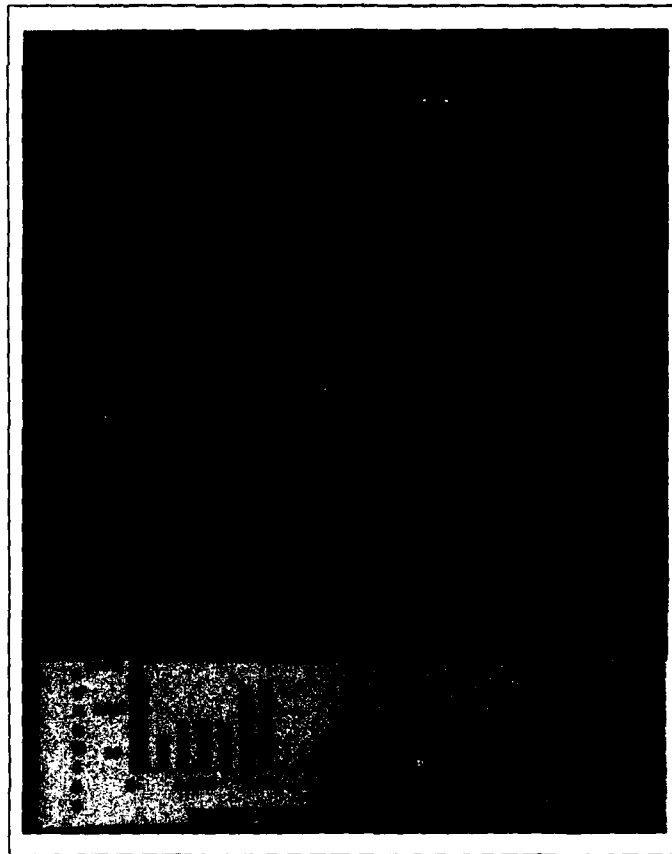
Figure 5.18. Moffett A_V Segmentation, $2.7 \leq D_f \leq 3.0$

Figure 5.18 is the histogram and contrast segmentation of the A_V image in Figure 5.17. This segmentation highlights those regions with estimated fractal dimensions between 2.7 and 3.0. This segmentation separates the city and the forested regions from all else in the scene.
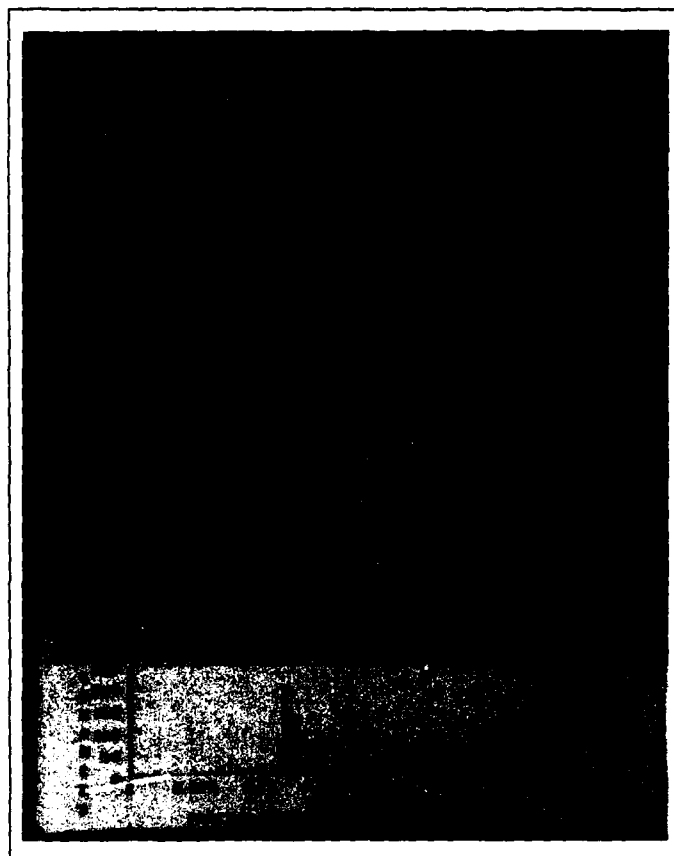
Figure 5.19. Moffett FULL Segmentation, $4.25 \leq D_f \leq 5.0$

Figure 5.19 is the histogram and the contrast segmentation of the five dimensional dataset, FULL, which includes δ, A_H and A_V returns form the $\chi = 5$, $\psi = -40$ degree transmitted wave. This segmentation highlights those regions with estimated fractal dimensions between 4.25 and 5.0. This segmentation separates the city from all else in the scene, including the main roads within the city and the forest regions to the north. This segmentation is the best example that demonstrates that the use of the complex data (phase and magnitude), as opposed to power returns only, does aid in the segmentation process.
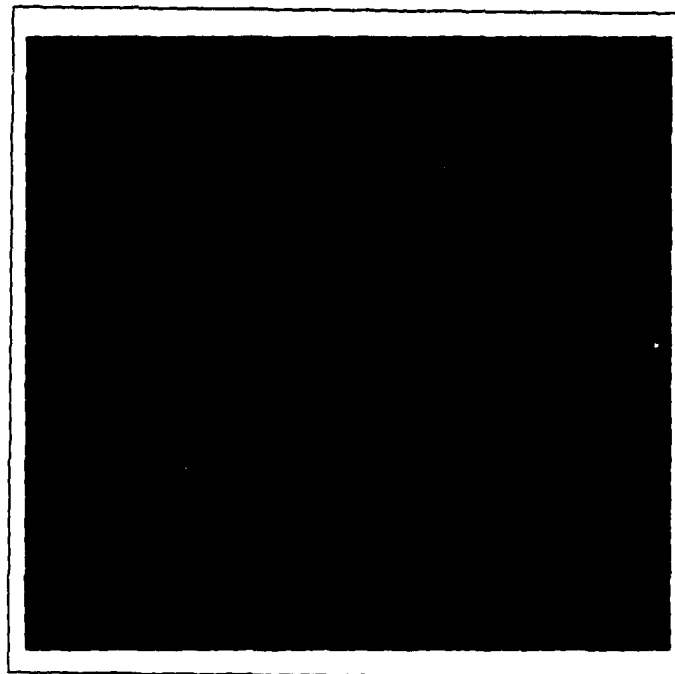
Figure 5.20. Bridge HH Image

Figure 5.20 is an image of the Golden Gate Bridge scene showing the power returns from an HH co-polarized return. The image clearly shows the city, bridge and natural regions.

Figure 5.21. Bridge HH Segmentation, $2.75 \leq D_f \leq 3.0$

Figure 5.21 is the histogram and contrast segmentation of the image in Figure 5.20. This segmentation highlights those regions with estimated fractal dimension between 2.75 and 3.0. It does a reasonable job of separating the man-made areas from the natural areas.
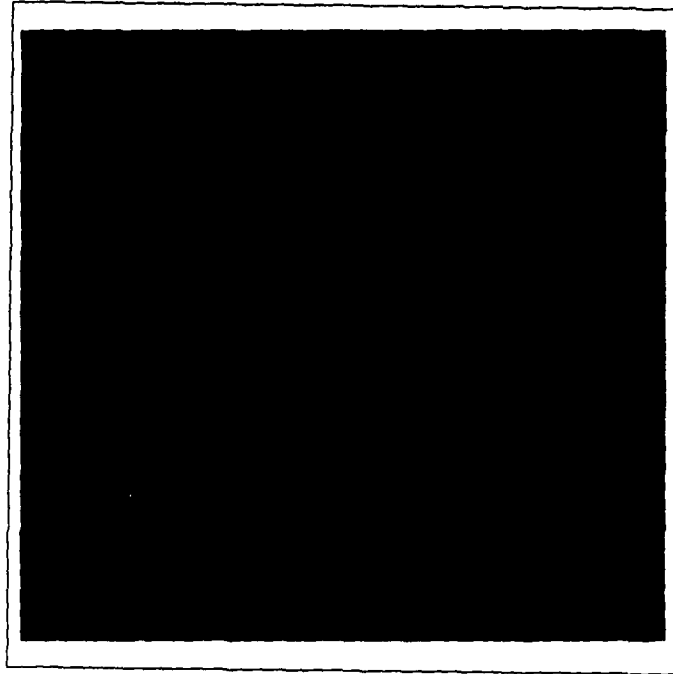
Figure 5.22. Bridge VV Image

Figure 5.22 shows the same scene generated from a VV power return. Once again the VV power return image shows more roughness in the water than does the HH power return image.
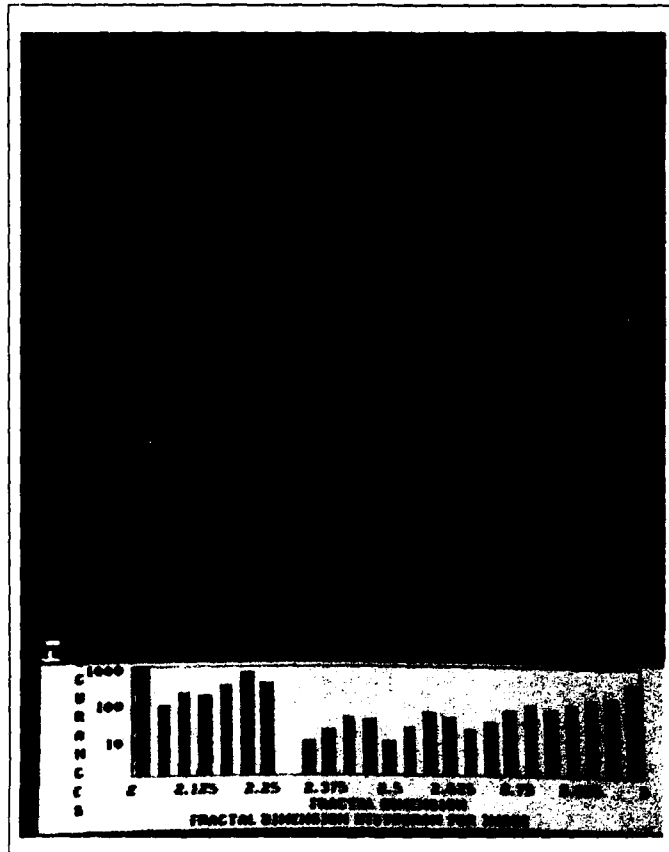
Figure 5.23. Bridge VV Segmentation, $2.9 \leq D_f \leq 3.0$

Figure 5.23 is the histogram and contrast segmentation for the image in Figure 5.22. This segmentation highlights those regions with estimated fractal dimension between 2.9 and 3.0. It separates the city from the other areas in the scene.
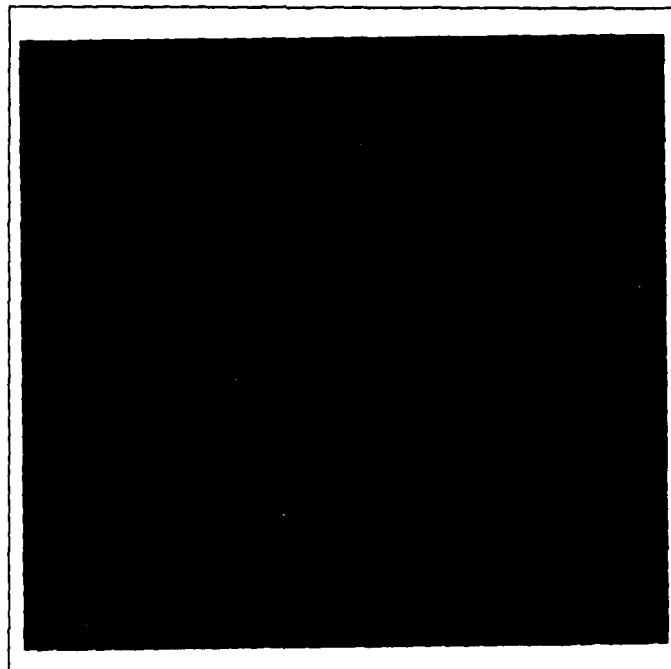
Figure 5.24. Bridge A_V Image

Figure 5.24 is the image generated from the dataset containing only A_V, the magnitude of the vertically polarized component of an elliptically polarized transmitted wave with $\chi = 10$ and $\psi = 40$ degrees. This image shows great detail about the scene.
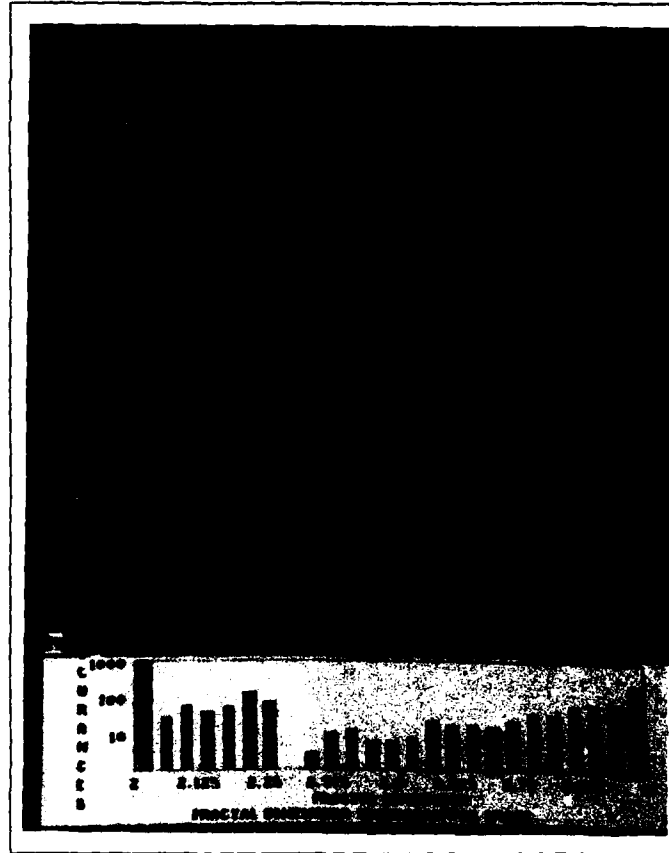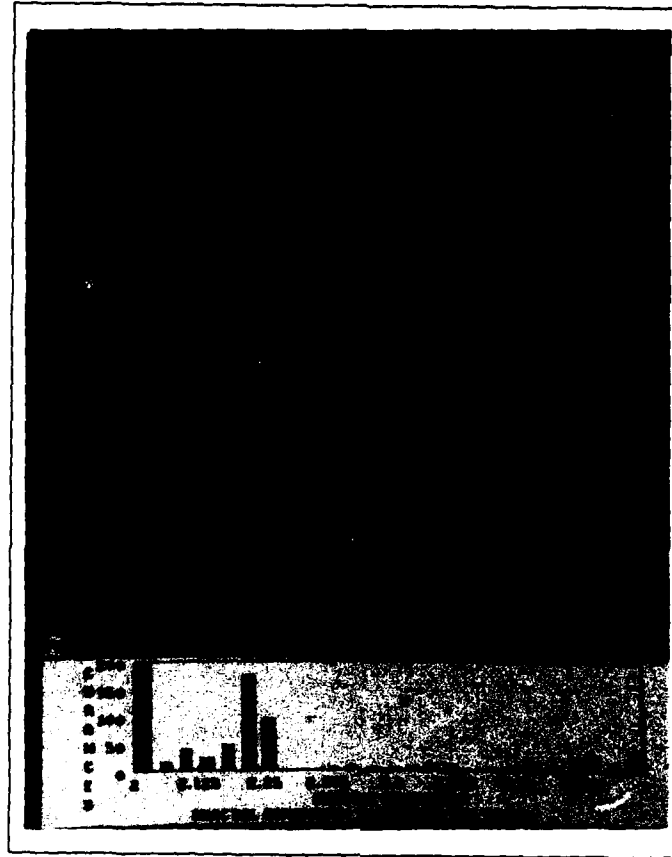
Figure 5.25. Bridge A_V Segmentation, $2.875 \leq D_f \leq 3.0$

Figure 5.25 is the histogram and contrast segmentation of the image in Figure 5.24. This segmentation highlights those regions with estimated fractal dimensions between 2.875 and 3.0. It does a fairly good job of separating the bridge from the rest of the scene.

Figure 5.26. Bridge FULL Segmentation, $4.25 \leq D_f \leq 5.0$

Figure 5.26 is the contrast segmentation and histogram of the five dimensional dataset, FULL, containing δ, A_H and A_V values for the $\chi = 10$, $\psi = 40$ transmitted polarization. The segmentation highlights regions with estimated fractal dimension between 4.25 and 5.0. It clearly separates the bridge from all else in the scene.
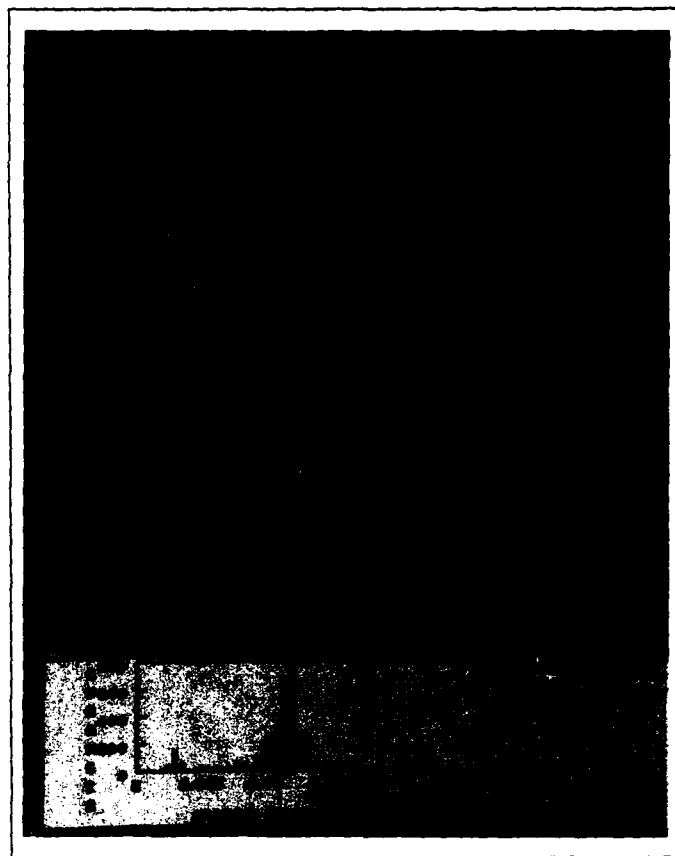
5.4.1 General Observations. Results of the fractal dimension estimations lend great support for the hypothesis that the "surfaces" generated by SAR returns could be modelled by fractal geometry. In all cases the estimates of fractal dimension fell within the expected intervals. All of the estimations were between 2.0 and the number of degrees of freedom for each specific dataset analyzed.

A study of the histograms for the power return segmentations and the magnitude return segmentations shows several similarities. In most cases a large number of regions had estimated fractal dimensions close to 2.25. Contrast segmentations of these regions showed that they usually represented regions containing boundaries or transitions between major areas within the scenes.

In almost every segmentation the regions with the highest estimated fractal dimensions represented man-made areas or very rough natural terrain. As predicted by classical Euclidean geometry, the flat surfaces in the scenes (ie. the water and the airfield) had estimated fractal dimensions approaching 2.0.

5.5 Objective Analysis

As stated in Chapter IV, data for each scene was available in nine different datasets. These datasets contained information arranged in varying Euclidean dimensions. It was desired to determine which of the available datasets provided the most information and thus the best segmentations of the scenes.

5.5.1 Figures of Merit. To effectively compare the quality of the segmentations it was necessary to define some figures of merit. Those chosen were: P_d, the probability of detection, P_{fa}, the probability of a false alarm, and Υ, the ratio of P_d/P_{fa}.

P_d was defined as the probability that the segmentation process would correctly identify and highlight regions within an area of interest. P_{fa} was the probability that the segmentation process would incorrectly identify and highlight regions within an area of conflict as part of the area of interest. Since it was desirable to simultaneously maximize P_d and minimize P_{fa}, the ratio of the two, $\Upsilon = P_d/P_{fa}$, was a convenient measure. Maximizing Υ was the same as simultaneously maximizing P_d and minimizing P_{fa}.

Those readers familiar with radar terminology will notice that P_d and P_{fa} are defined here just as they are in conventional radar systems analysis [18:27].

5.5.2 AOI and AOC. The objective analysis was performed by choosing an area of interest (AOI) and an area of conflict (AOC) which would often have an estimated fractal dimension close to that of the area of interest. Specifically, the AOIs chosen for each scene were the city regions (the bridge was also included in the appropriate scenes). The AOCs were the forested or rough terrain areas in each scene.

These areas were chosen in part because the ability to differentiate between man-made and natural regions was one of the original intents of this thesis. Another reason was that these regions consistently had estimated fractal dimensions at the uppermost end of the histograms generated for the segmentations. This meant that both the AOIs and the AOCs could be separated from all else in the scenes by selecting to display segmentations with only those fractal dimensions greater than a minimum threshold value. The upper bound on the intervals of display was always equal to number of degrees of freedom in the particular dataset under consideration. This was fortuitous because it meant that the interval of fractal dimensions of interest could be defined by only one number, the lower bound, instead of both a lower and an upper bound. This lower bound, or threshold, was designated τ and was the independent variable which defined each contrast segmentation used in the objective analysis. The selection of a segmentation with a lower bound τ also necessarily defined a specific P_d and P_{fa}. Thus every different segmentation could be specified by either τ or a combination of P_d and P_{fa}.

Neither this threshold, τ, nor the figure of merit, Υ, should be confused with the test statistics or likelihood ratios used in conventional detection and estimation theory [6:292-293] [18:27-29]. Although they are similarly defined, they cannot be similarly interpreted for this application.

5.5.3 Analysis Procedure. The number of 8x8 pixel regions that covered the AOIs and the AOCs in the images were counted (estimated). The segmentations were then performed and again the number of 8x8 pixel regions relating to both the area of interest

and the area of conflict were counted. (These estimates were thought to be well within 10% of the actual number of regions.)

P_d was computed as the number of regions relating to the area of interest in the segmentation divided by the number of regions covering the area of interest in the image. P_{fa} was the number of regions relating to the areas of conflict displayed in the segmentation divided by 4096 (the total number of regions in the images) minus the number of regions relating to the area of interest in the images.

$$P_d = \frac{\text{\# of regions in AOI in segmentation}}{\text{\# of regions in AOI in image}}$$

$$P_{fa} = \frac{\text{\# of regions in AOC in segmentation}}{(4096 - \text{\# of regions in AOI in image})}$$

(5.1)

Various segmentations, with differing τ, were then observed for each dataset. P_d, P_{fa} and Υ were computed for each segmentation. Comparisons were made between the different segmentations derived from a single dataset and between the best segmentation of each dataset (defined by maximum Υ) with the best from the other eight datasets.

The "best" segmentations for each of the nine datasets are pictured in Figures 5.27 through 5.53 in order of ascending quality (Υ) for each of the three scenes. Data from this analysis is shown in Table 5.1 and the final results of the comparisons are summarized in Table 5.2.

Table 5.1 shows values of τ and Υ for each of the nine different datasets for each scene. Rankings of the quality of segmentations made from these datasets are given for each scene. These rankings are based on comparing Υ values within each scene. The final rankings represent an averaging of the rankings of each dataset over the three scenes. The rankings for each scene and the final rankings are tabulated in descending order in Table 5.2.

5.5.4   General Observations. Table 5.2 shows that, on average, the higher the dimension of the dataset being segmented, the better the segmentation will be. The five

Dataset	Moffett			San Fran			Bridge			Ave Rank	Final Rank
	τ	Υ	Rank	τ	Υ	Rank	τ	Υ	Rank		
HH	2.97	9.0	8	2.95	11.8	5	2.96	12.5	4	5.7	6,7
VV	2.96	7.5	9	2.98	9.4	7	2.93	8.3	8	8.0	9
HV	2.04	39.9	4	2.09	11.7	6	2.30	11.7	5	5.0	4
POL	3.75	39.0	5	3.75	37.1	2	3.55	10.7	7	4.7	3
3POL	3.8	71.0	2	3.75	42.8	1	3.85	10.9	6	3.0	2
δ	2.96	56.9	3	2.94	12.2	4	2.98	7.7	9	5.3	5
A_H	2.96	11.8	6	2.875	4.75	9	2.92	69.2	3	6.0	8
A_V	2.96	11.0	7	2.98	6.8	8	2.92	89.0	2	5.7	6,7
FULL	4.25	179	1	4.4	14.2	3	3.875	98 0	1	1.7	1

Table 5.1. Comparison of Datasets by Objective Analysis

dimensional datasets, FULL, and 3POL are ranked as best and second best, respectively. The four dimensional dataset, POL, is ranked third out of the nine different datasets.

Comparisons of the final rankings of the three dimensional datasets shows that the cross-polarized power returns lead to better segmentations than do the co-polarized power returns or the magnitude or phase returns. They also indicate that the datasets containing information about the horizontally polarized returns may be more useful than are the vertically polarized returns. These observations, however, are not intuitive and may be unique to these scenes and AOC and AOI choices. As such, they are not interpreted as generally applicable.

The quality of the segmentations of the δ datasets is a testimony to the power of the fractal dimension segmentation process. Although the images generated from these datasets are generally unrecognizable, the information which they contain about the scene is revealed after segmentation. The segmentations are often more recognizable than the images!

Upsilon was a useful figure of merit for comparing the value of datasets depicting the same scene, but was not useful for comparisons between differing scenes. For exam-

ple, a segmentation with $\Upsilon = 10$ is "better" than a segmentation with $\Upsilon = 5$ if the segmentations were of the same scene. This was not necessarily true if the two segmentations represented different scenes. Thus no conclusions could be made about what types of scenes may or may not lend themselves to a fractal dimension segmentation.

Table 5.1 shows that the same value of τ did not identify segmentations of similar quality (same Υ) for every scene. To achieve a given Υ, in the different scenes, the threshold, τ, had to be empirically determined. This meant that a single threshold value could not be preprogrammed into an automated segmentation algorithm to achieve segmentations of some specified quality. This threshold value must be adaptively determined for each different scene.

Some of the "best" segmentations had a calculated P_d of less than 0.5. Radar purists may be alarmed at the use of a $P_d \leq 0.5$. They should not be. In a radar system, P_d is a measure of the system's ability to determine whether or not a target exists. A radar system yielding a P_d of less than 0.5, according to classical detection theory, is interpreted as worse than a coin flip at determining the existence of a target. These systems actually make the wrong decision most of the time. To correct this problem, the final decision can be reversed so that 've system will then make the correct decision most of the time.

A P_d of less than 0.5, as defined in this segmentation process, can not be interpreted in the same manner. The segmentation P_d does not determine a yes/no, target present/target not present, decision. Instead, it provides a measure of the percentage of the target area (that is known to exist) that is correctly selected by the segmentation process. The definition of a "good" segmentation (defined by maximum Υ) makes no limitations on the acceptable values of P_d. The interpretation must be that a "good" segmentation between an AOI and a AOC can be made even though less than one-half of the total AOI is represented in the final segmentation.

It is interesting to note that almost without exception, the threshold, τ which determined the "best" segmentation under the subjective analysis criteria was within approximately seven percent of the τ which determined the "best" segmentation under the objective analysis. This fact can be attributed to either the great strength of the human

5-33

visual system to segment images or, to biases introduced into the subjective analysis due to the analyzer's (the author's) a priori knowledge of the ground truth of the scenes.

Rank	Moffett	San Fran	Bridge	Final
1	FULL	3POL	FULL	FULL
2	3POL	POL	A_V	3POL
3	δ	FULL	A_H	POL
4	HV	δ	HH	HV
5	POL	HH	HV	δ
6	A_H	HV	3POL	A_V,HH
7	A_V	VV	POL	A_V,HH
8	HH	A_V	VV	A_H
9	VV	A_H	δ	VV

Table 5.2. Ranking of Datasets
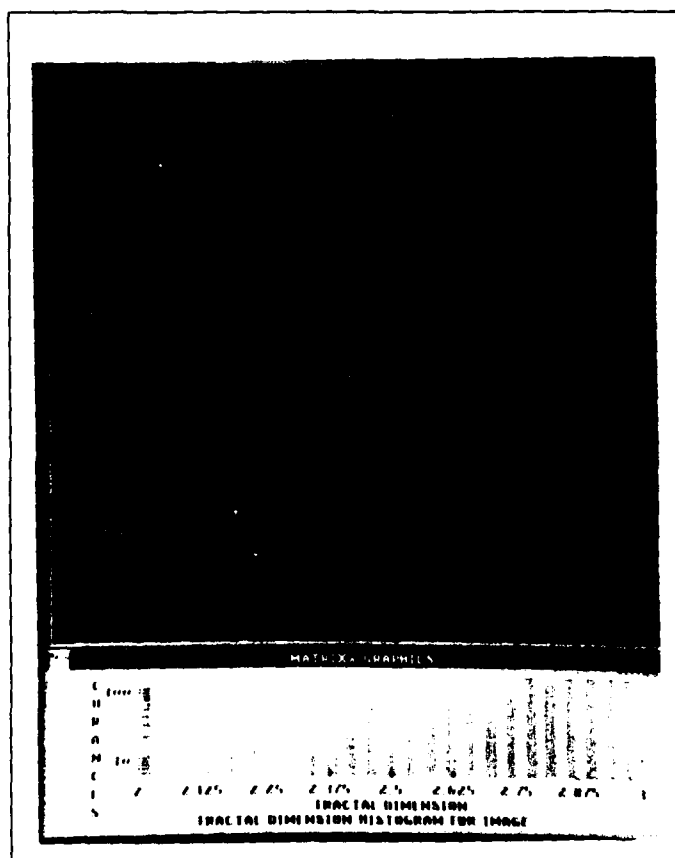
Figure 5.27. Moffett VV Segmentation, $2.96 \leq D_f \leq 3.0$, $\Upsilon = 7.5$
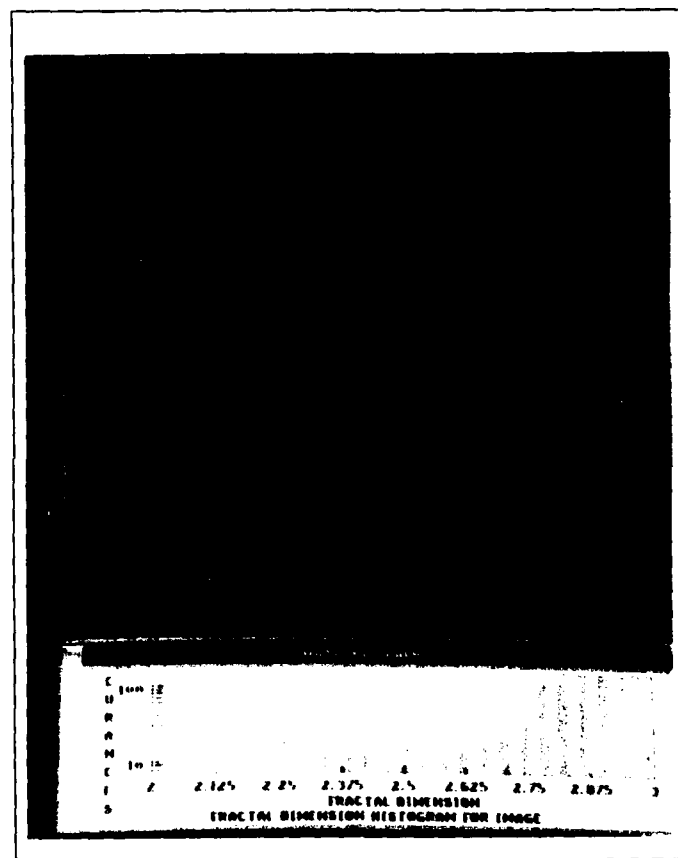
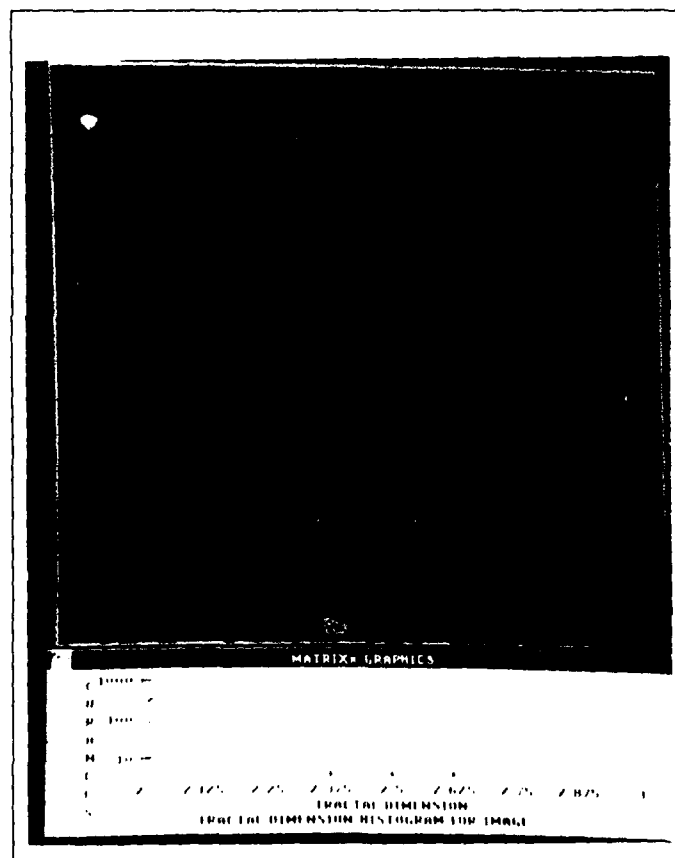Figure 5.28. Moffett HH Segmentation, $2.97 \leq D_f \leq 3.0$, $\Upsilon = 9.0$

Figure 5.29. Moffett A_V Segmentation, $2.96 \leq D_f \leq 3.0$, $\Upsilon = 11.0$
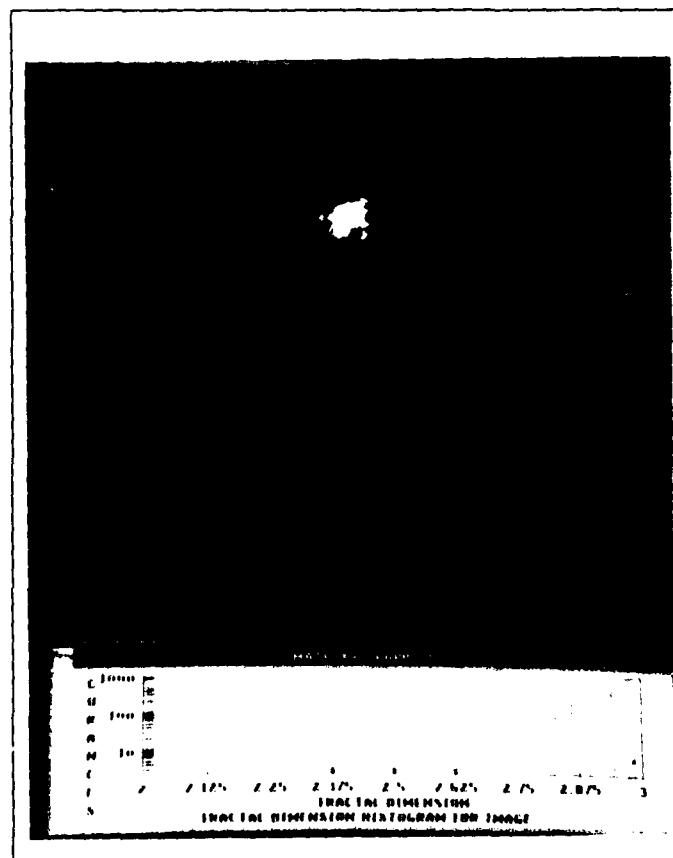
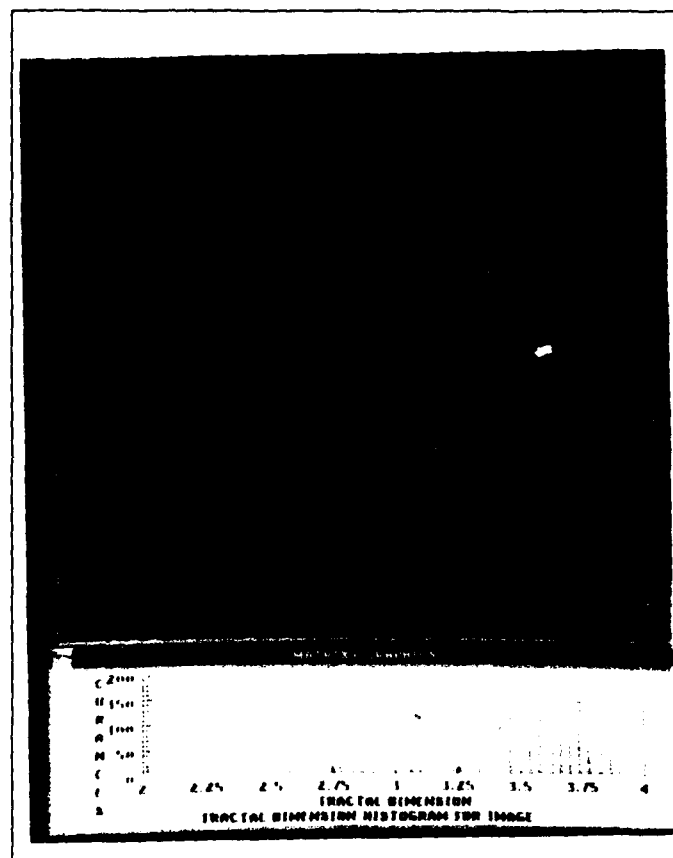Figure 5.30. Moffett A_H Segmentation, $2.96 \leq D_f \leq 3.0$, $\Upsilon = 11\ 8$

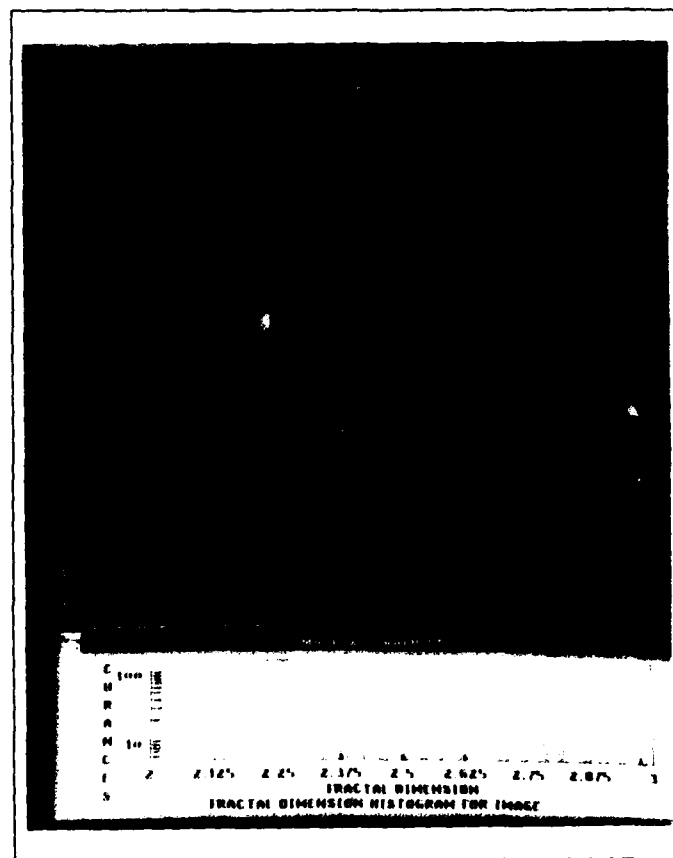Figure 5.31. Moffett POL Segmentation, $3.75 \leq D_f \leq 4.0$, $\Upsilon = 39.0$

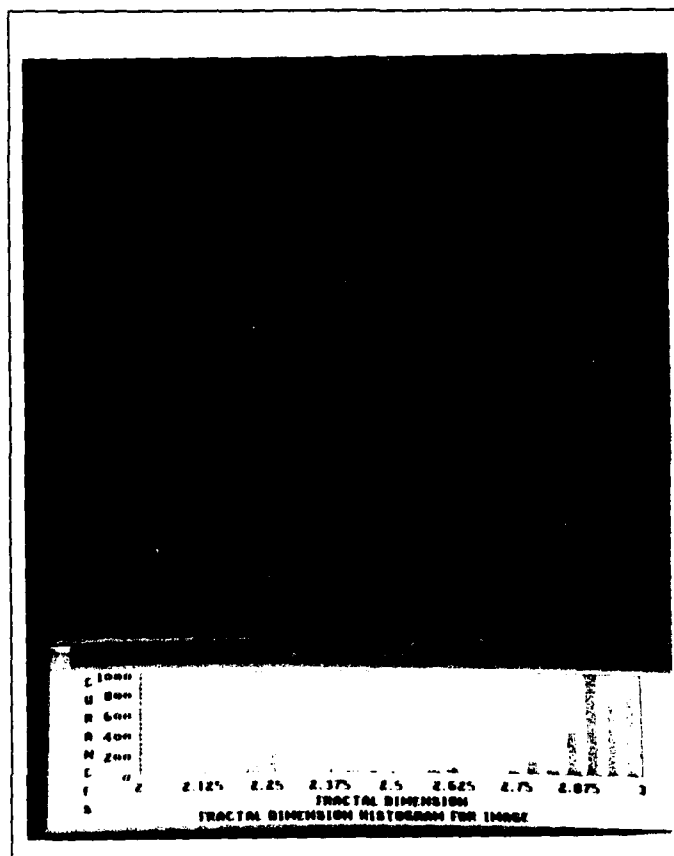Figure 5.32. Moffett HV Segmentation, $2.04 \leq D_f \leq 3.0$, $\Upsilon = 39.9$

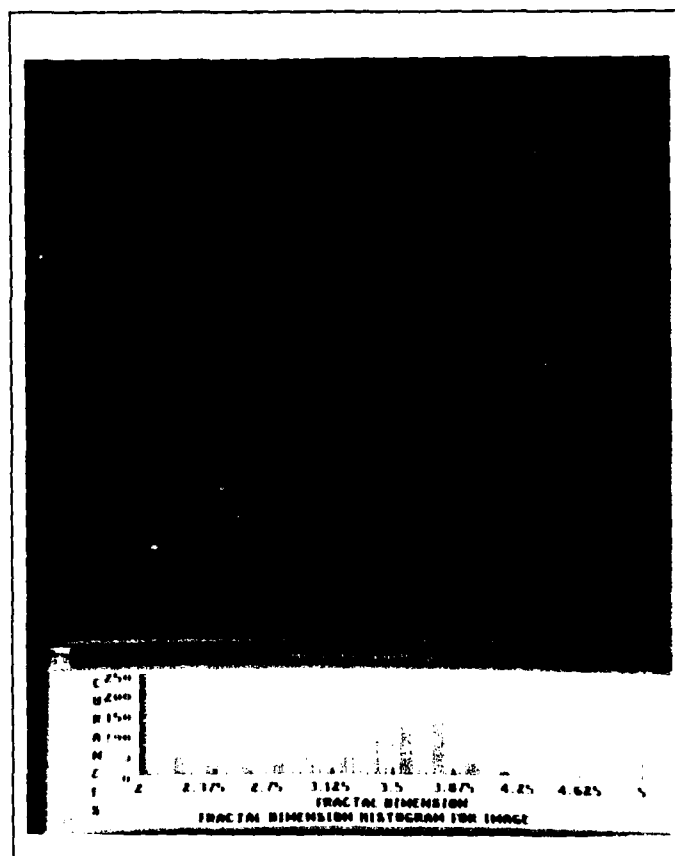Figure 5.33. Moffett δ Segmentation, $2.96 \leq D_f \leq 3.0$, $\Upsilon = 56.9$

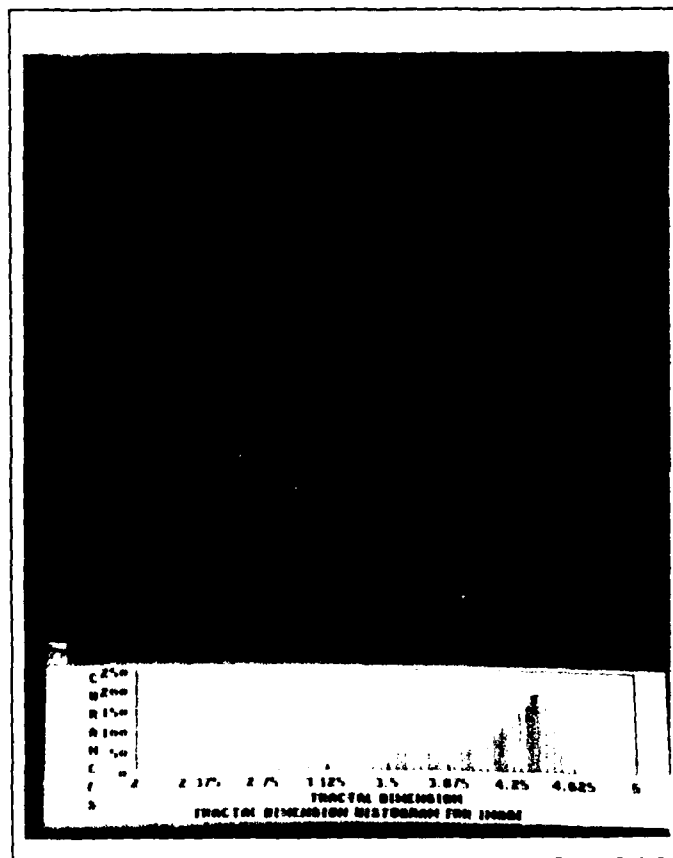Figure 5.34. Moffett 3POL Segmentation, $3.8 \leq D_f \leq 5.0$, $\Upsilon = 71.0$

Figure 5.35. Moffett FULL Segmentation, $4.25 \leq D_f \leq 5.0$, $\Upsilon = 179.0$

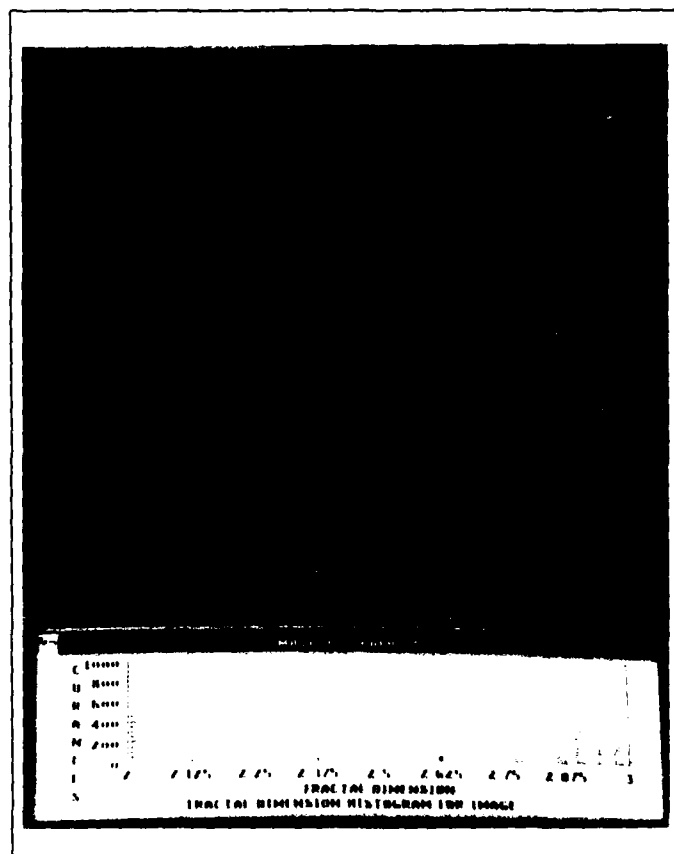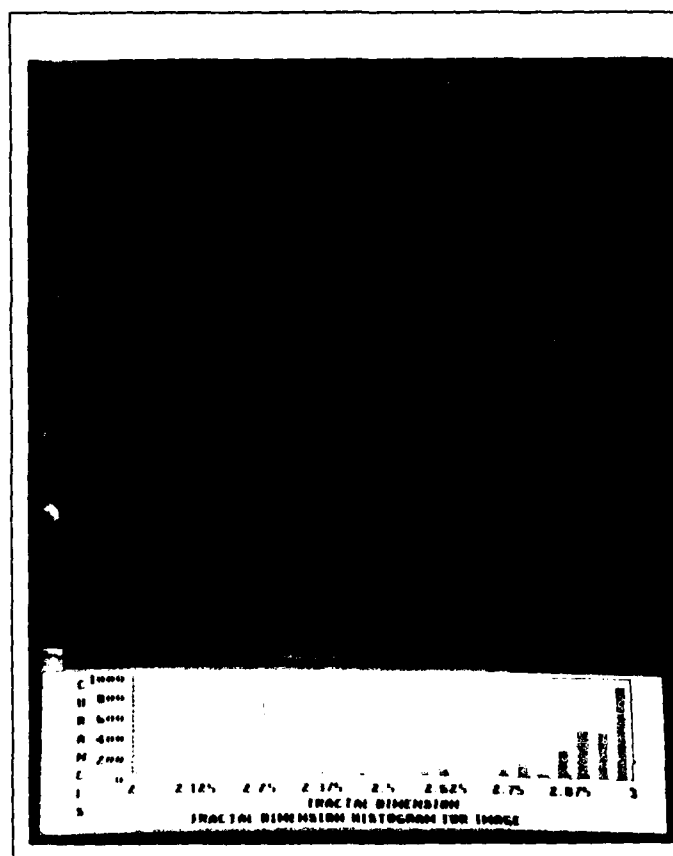Figure 5.36. San Fran A_H Segmentation, $2.875 \leq D_f \leq 3.0$, $\Upsilon = 4.75$

Figure 5.37. San Fran A_V Segmentation, $2.98 \leq D_f \leq 3.0$, $\Upsilon = 6.8$

Figure 5.38. San Fran VV Segmentation, $2.98 \leq D_f \leq 3.0$, $\Upsilon = 9.4$
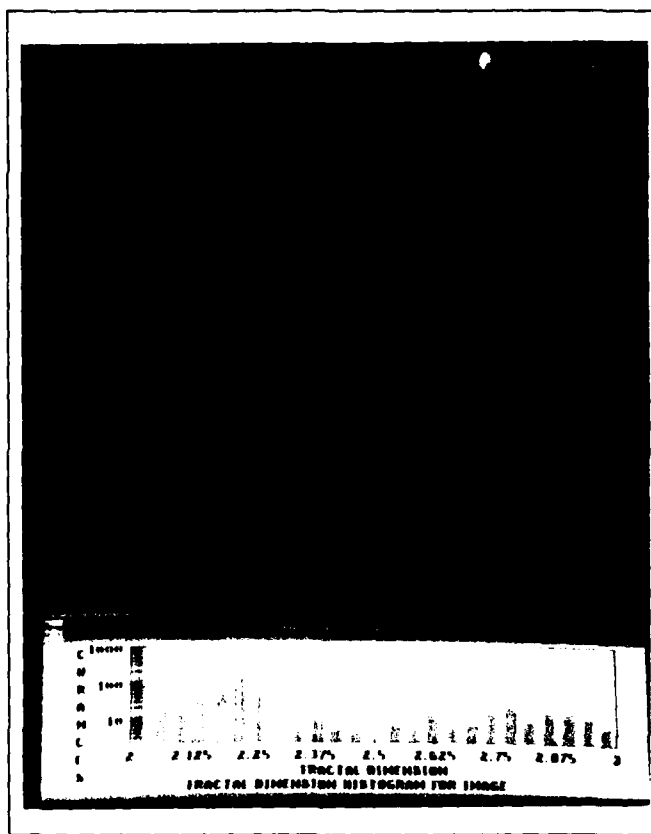
Figure 5.39. San Fran HV Segmentation, $2.09 \leq D_f \leq 3.0$, $\Upsilon = 11.7$

5-48
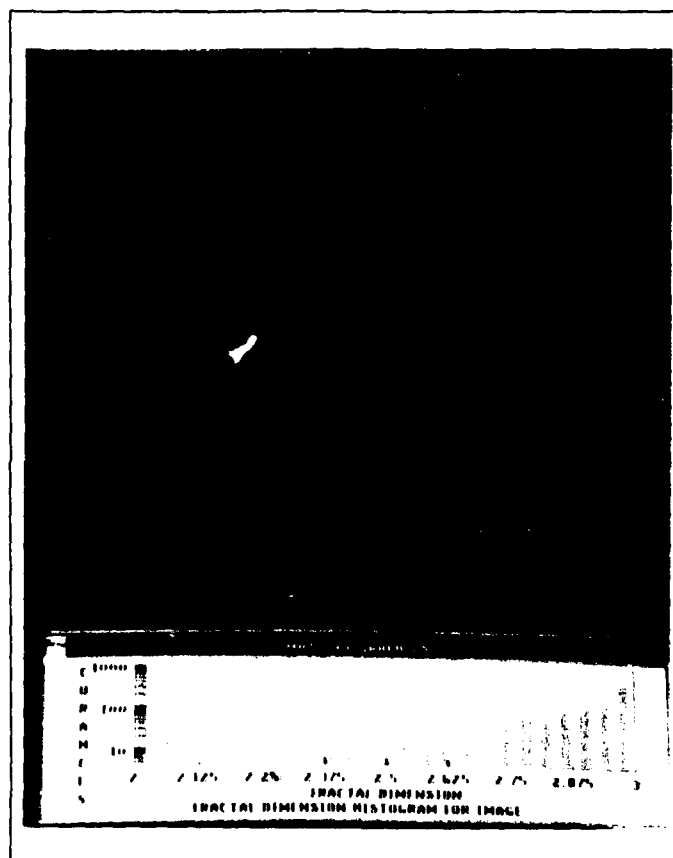
Figure 5.40. San Fran HH Segmentation, $2.95 \leq D_f \leq 3.0$, $\Upsilon = 11.8$
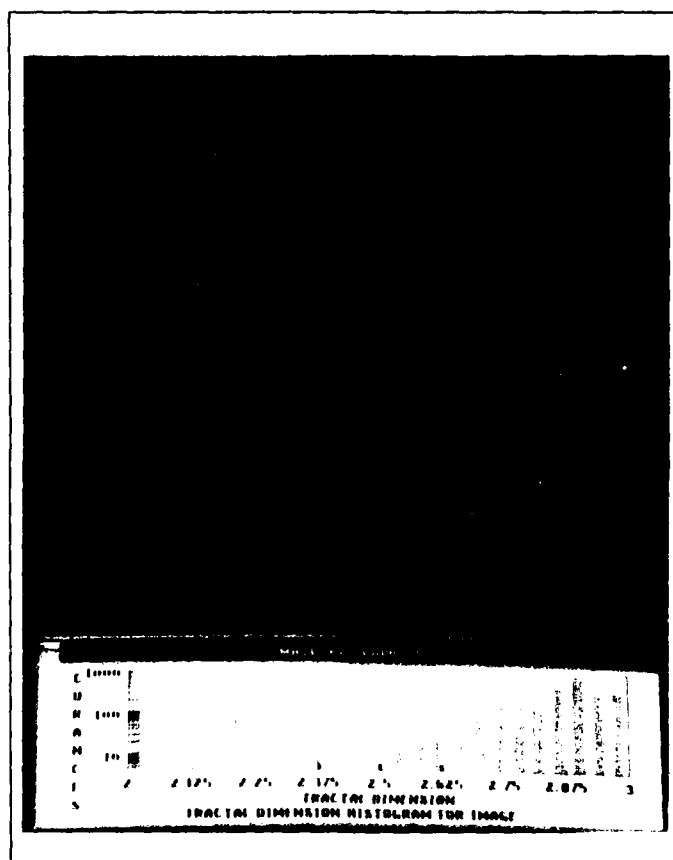
Figure 5.41. San Fran δ Segmentation, $2.94 \leq D_f \leq 3.0$, $\Upsilon = 12.2$
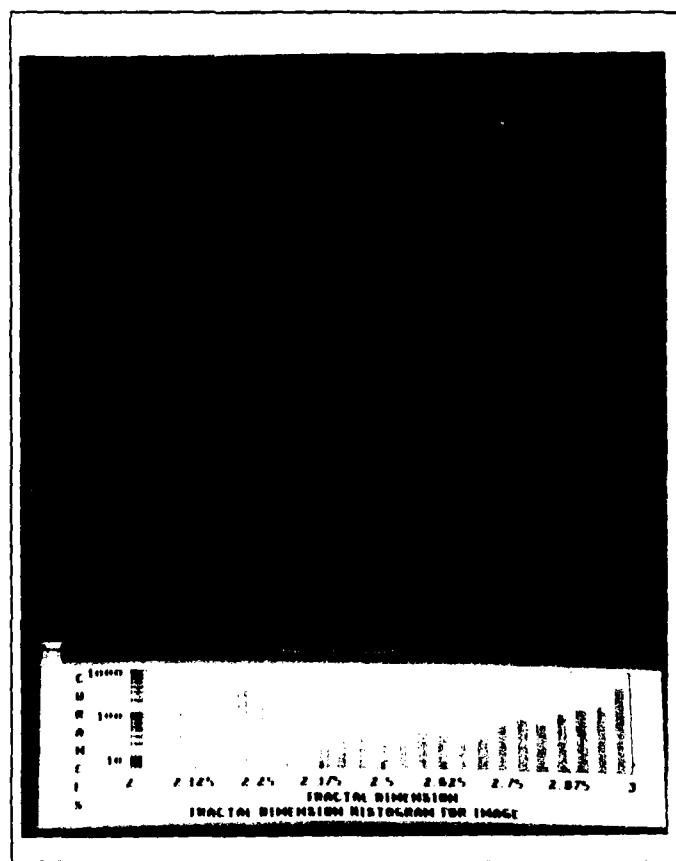
Figure 5.42. San Fran FULL Segmentation, $4.4 \leq D_f \leq 5.0$, $\Upsilon = 14.2$
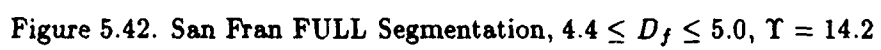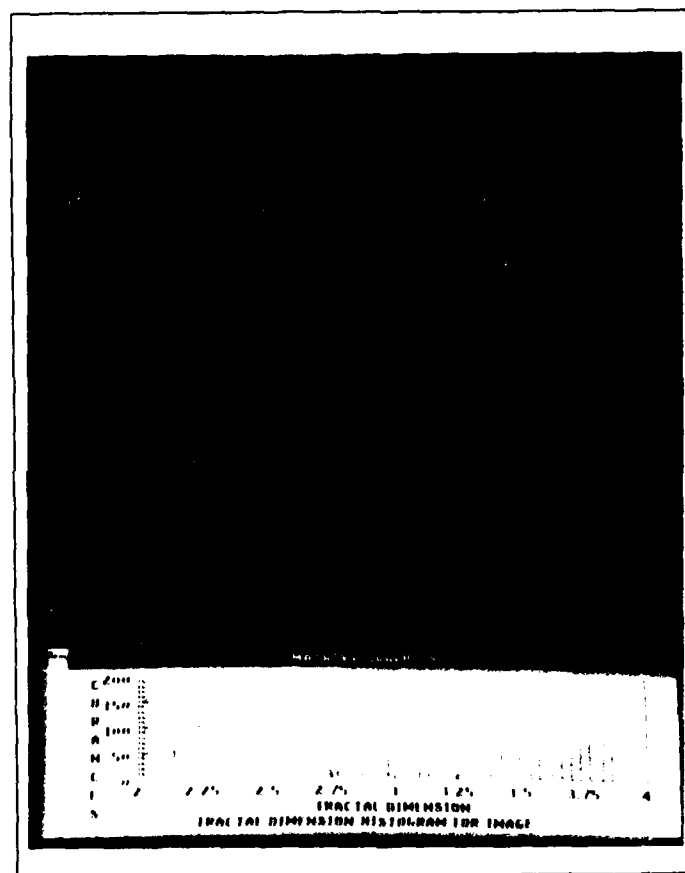
Figure 5.43. San Fran POL Segmentation, $3.75 \leq D_f \leq 4.0$, $\Upsilon = 37.1$
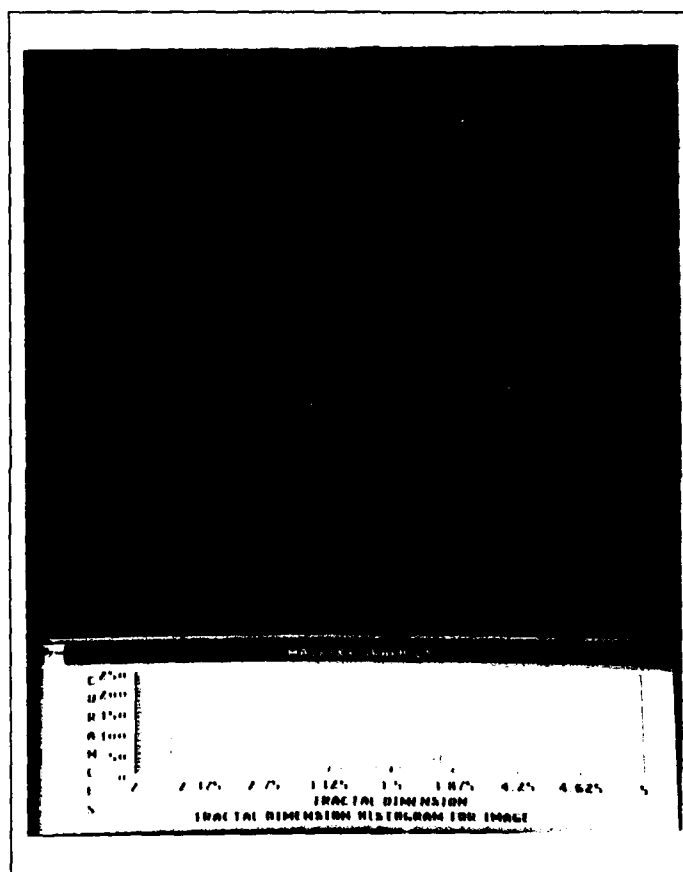
Figure 5.44. San Fran 3POL Segmentation, $3.75 \leq D_f \leq 5.0$, $\Upsilon = 42.8$

Figure 5.45. Bridge δ Segmentation, $2.98 \leq D_f \leq 3.0$, $\Upsilon = 7.7$

Figure 5.46. Bridge VV Segmentation, $2.93 \leq D_f \leq 3.0$, $\Upsilon = 8.3$

Figure 5.47. Bridge POL Segmentation, $3.55 \leq D_f \leq 4.0$, $\Upsilon = 10.7$

Figure 5.48. Bridge 3POL Segmentation, $3.85 \leq D_f \leq 5.0$, $\Upsilon = 10.9$

Figure 5.49. Bridge HV Segmentation, $2.3 \leq D_f \leq 3.0$, $\Upsilon = 11.7$

Figure 5.50. Bridge HH Segmentation, $2.96 \leq D_f \leq 3.0$, $\Upsilon = 12.5$
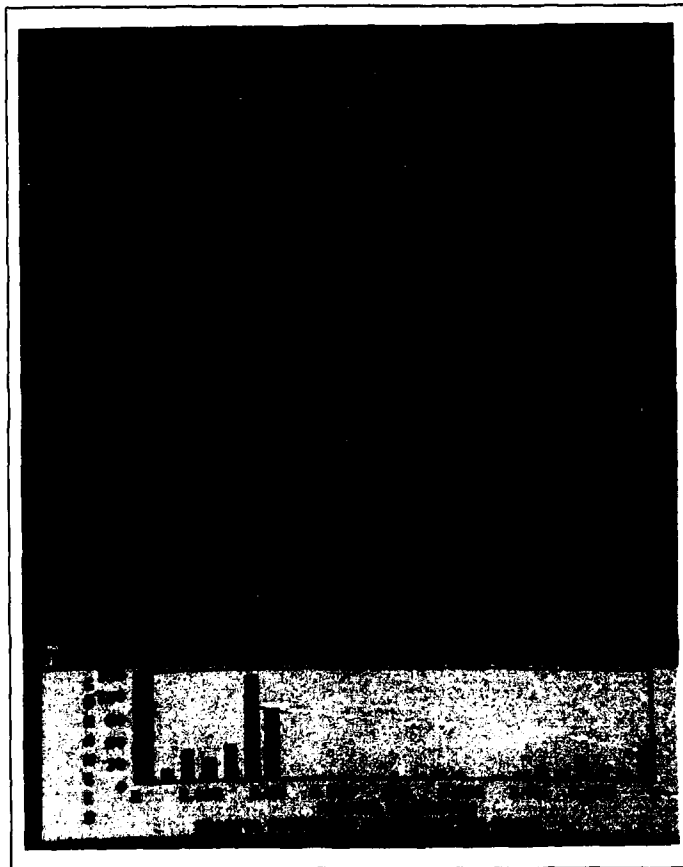
Figure 5.51. Bridge A_H Segmentation, $2.92 \leq D_f \leq 3.0$, $\Upsilon = 69.2$
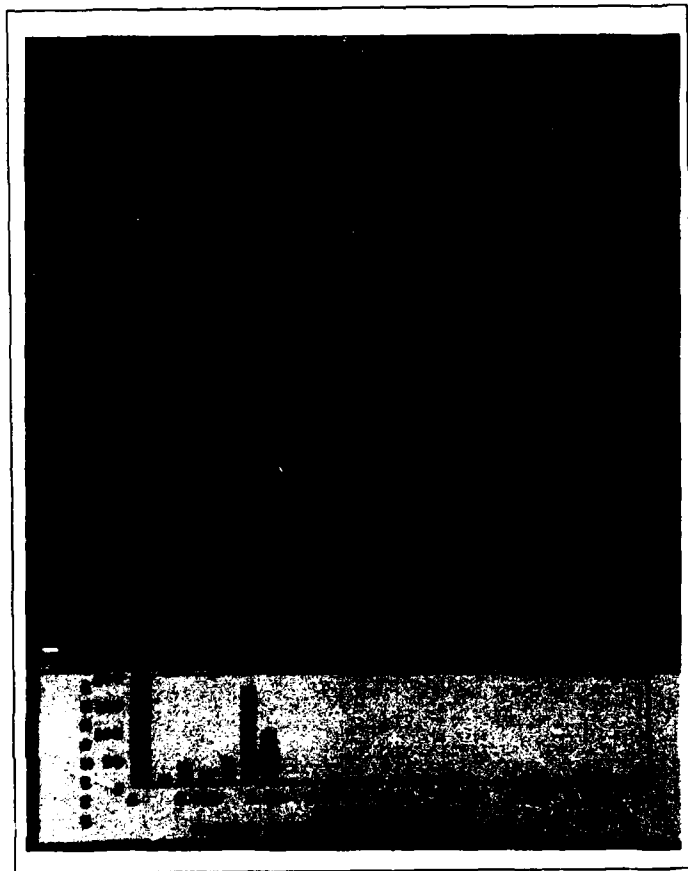
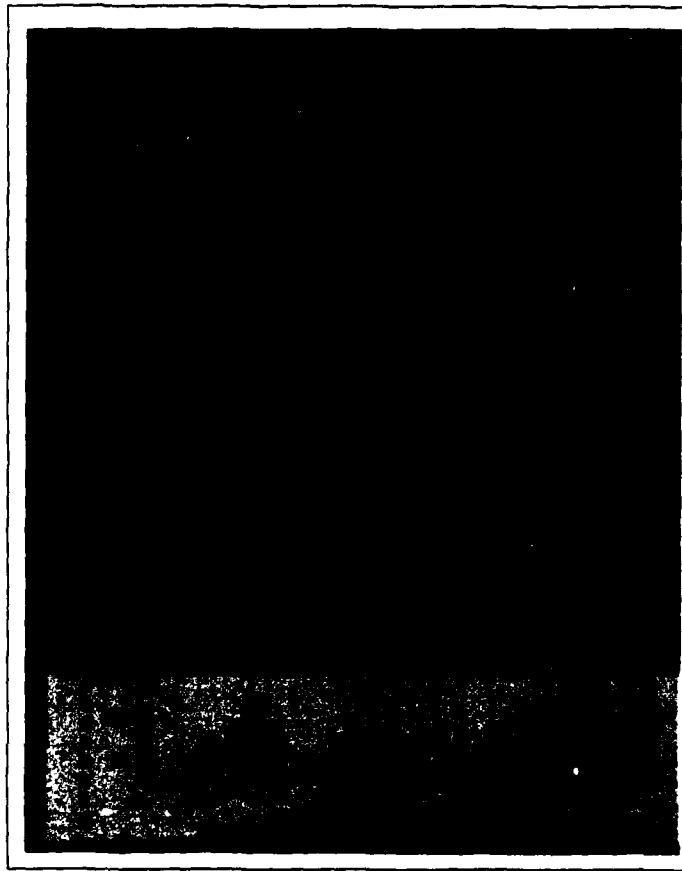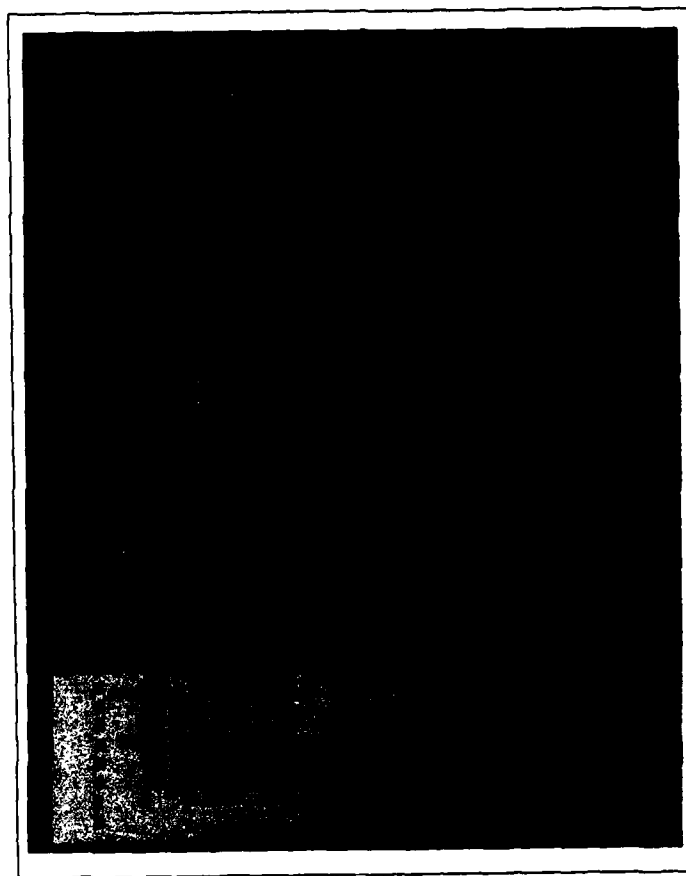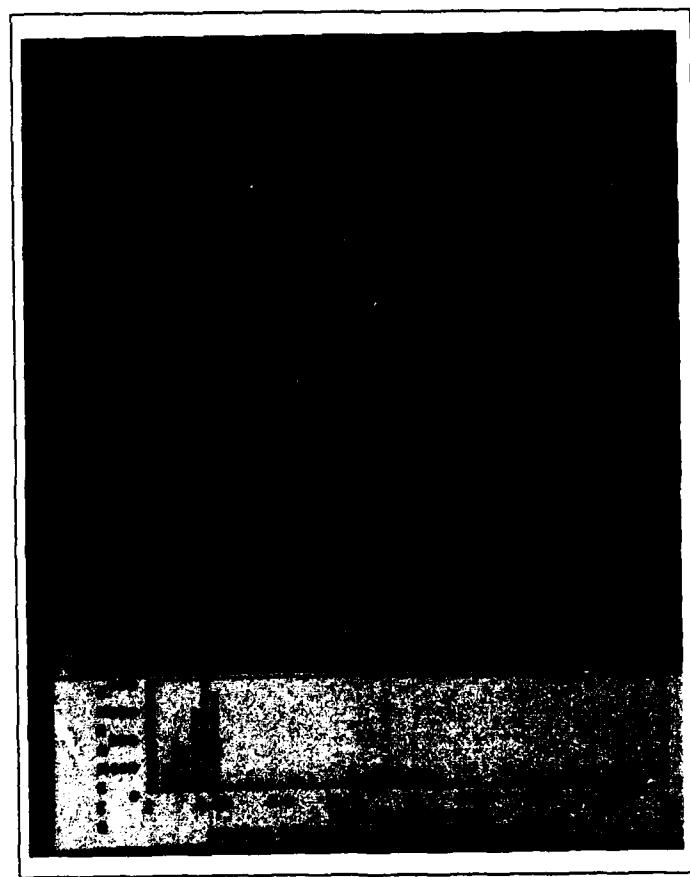Figure 5.52. Bridge A_V Segmentation, $2.92 \leq D_f \leq 3.0$, $\Upsilon = 89.0$
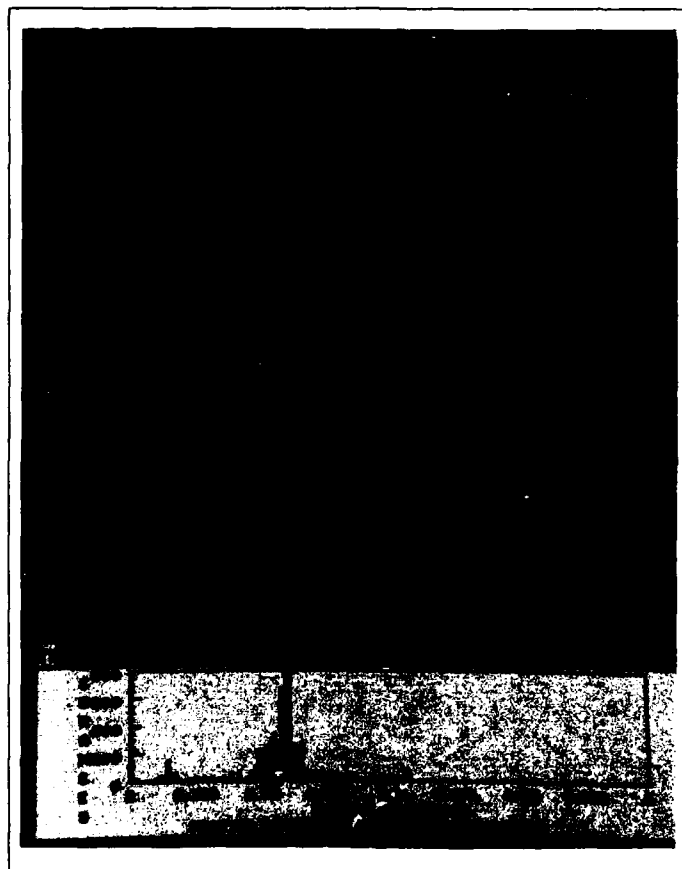
Figure 5.53. Bridge FULL Segmentation, $3.875 \leq D_f \leq 5.0$, $\Upsilon = 98.0$
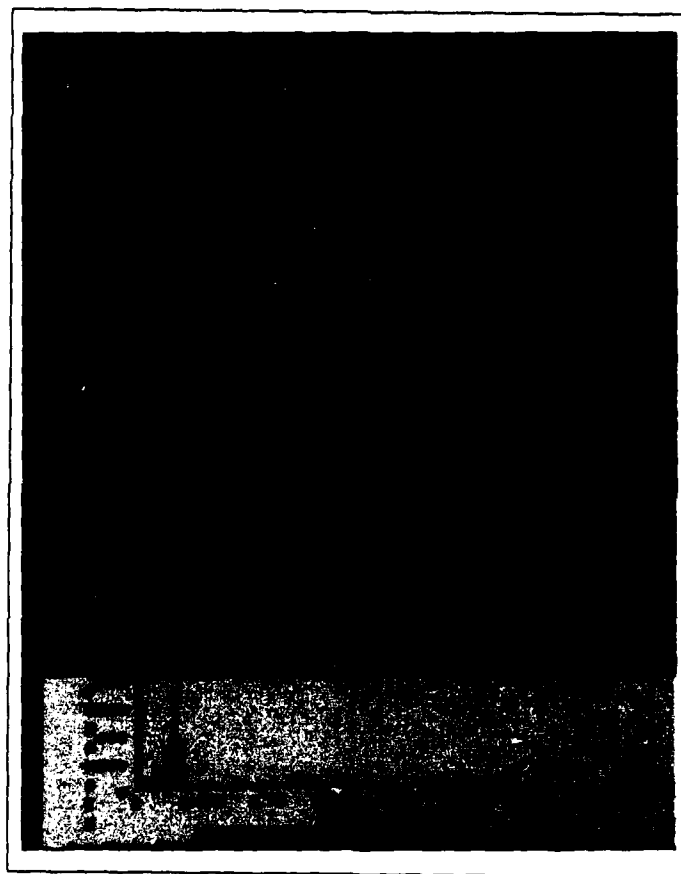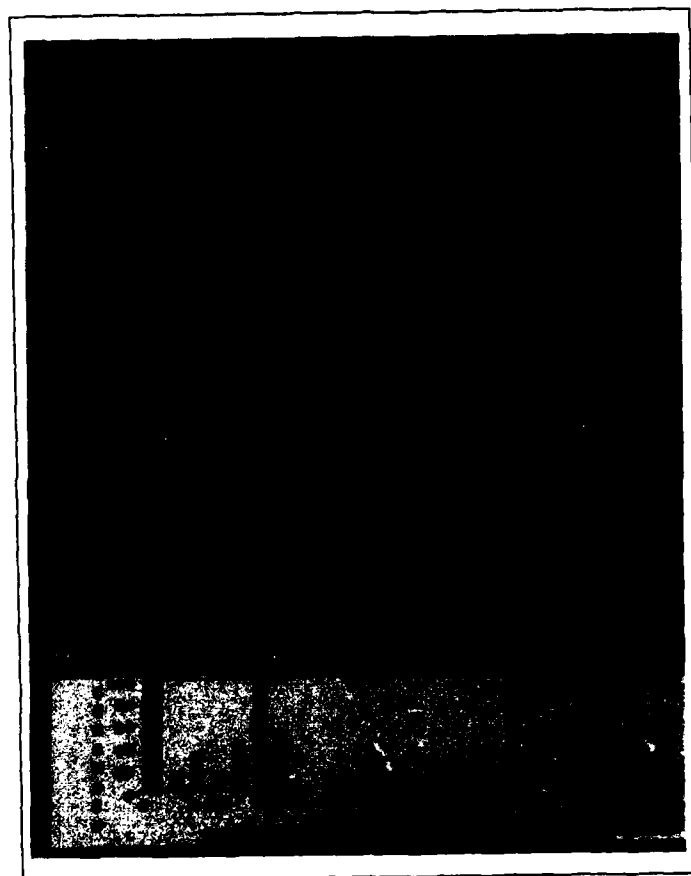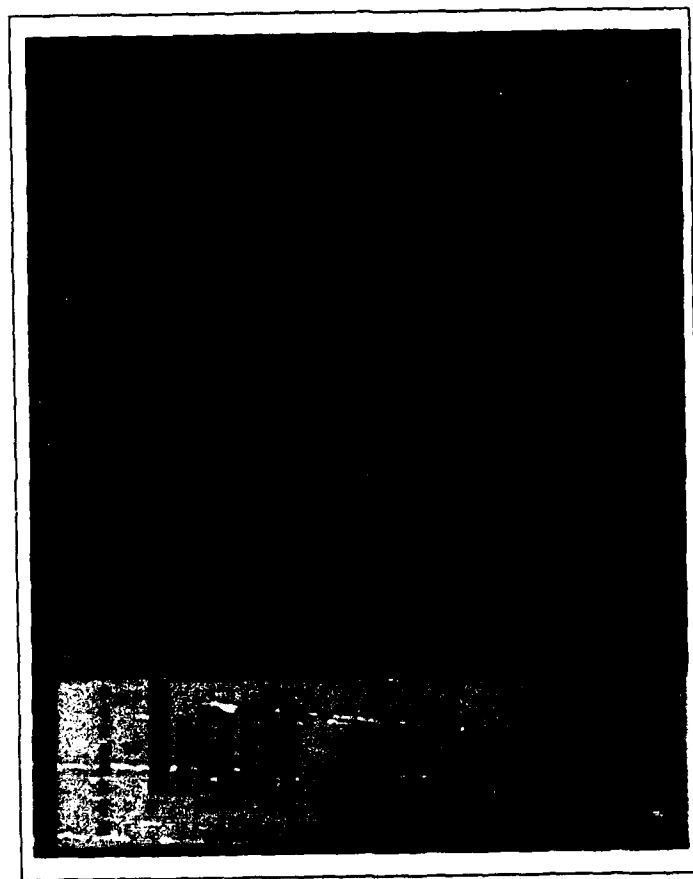
VI. Conclusions and Recommendations

6.1 Overview

This chapter contains the conclusions made from the work done in this thesis. It also contains recommendations from the author regarding future studies in the area of fractal geometry segmentation of images.

6.2 Conclusions

Fractal geometry techniques provide a valid and useful approach to segmenting polarimetric SAR images. The quality and utility of these segmentations differs with varying polarizations and with varying combinations of complex data. This conclusion is supported by the results of both the subjective and objective analyses described in Chapter V.

The use of the complex data (phase and magnitude) of the SAR returns yields more information about the target scene than does the use of only the magnitude or power returns. This conclusion is made as a result of the objective analysis described in Chapter V. It is clear that the higher Euclidean dimension of the dataset being segmented, the "better" the segmentation will be. Intuitively, the more information fed into the segmentation process, the better job it will do.

There is nothing unique in the methodology of this thesis which limits the fractal dimension segmentation algorithms to SAR data only. Any image, from any source (ie. photographs, digital data, etc.), which can be displayed using intensity values can be segmented by these algorithms.

6.3 Recommendations

The following recommendations are made to anyone pursuing studies in the use of fractal geometry to segment images.

6.3.1 Preprocessing. Some preprocessing of the image data may aid in the segmentation or object identification processes. This preprocessing could locate and enhance the boundaries between different areas in an image. Estimations of fractal dimension could be

made for only those regions which lie completely within these defined areas. In this way, estimates of the regions which contain boundaries will not skew or blend segmented areas into each other. Greater contrast between distinct areas would result.

Edge enhancement might also help in making estimates of the fractal dimensions of these same boundaries. The boundaries themselves could be considered as curves in Euclidean two-space. The fractal dimensions of these boundaries might give some aid in identifying what may be contained within the bounded area. For example, a boundary or edge with a fractal dimension of approximately 1.0 might indicate a man-made area, or a boundary with a higher fractal dimension, say 1.68, might indicate a ccastline or forest edge.

6.3.2 *Optimum Region Size.* Some work should be done to determine the optimum region size for use in the segmentation process. The 8x8 pixel regions used in this thesis were chosen for nonrigorous reasons. Previous experimenters have also pondered this same question without finding a definitive answer.

6.3.3 *Optimum Polarization.* A study should be undertaken to determine what the optimum polarizations are for segmenting SAR data by fractal geometry. Some work has already been accomplished to determine the optimum polarizations for enhancing contrast within the SAR images [16:988-990] [34:539-543] and to reduce the effects of speckle noise in the images [21]. This same type of effort might prove useful if the optimization was done specifically with image segmentation in mind instead of simply image display.

6.3.4 *Optimum Normalization.* Follow-on work to this thesis might also include studies to determine the optimum techniques for normalizing the image data prior to display. Normalization in this thesis was done on a empirical basis. Clearly there is a more rigorous method.

6.4 *Summary*

Fractals are wonderfully powerful tools with which to study nature. Their full potential as an aid to scene segmentation and object identification has not yet been tapped.

Bibliography

1. George Nickel, Public Colloquium, 20 September 1989, School of Engineering, Air Force Institute of Technology.

2. R. Badii and A. Politi. Hausdorff dimension and uniformity factor of strange attractors. *Physical Review Letters*, 52 NO. 19, May 7 1984.

3. Michael F. Barnsley. Fractal modelling of real world images. In *SIGGRAPH '87, Fractals: Introduction, Basics and Perspectives*, 1987.

4. Michael F. Barnsley. *Fractals Everywhere*. Academic Press Inc., 1250 Sixth Avenue, San Diego, CA 92101, 1988.

5. P.A. Burrough. The application of fractal ideas to geophysical phenomena. *The Institute of Mathematics and its Applications*, 20, March/April 1984.

6. J.V. DiFranco and W.L. Rubin. *Radar Detection*. Artech House, Inc, 685 Canton St., Norwood, Mass 02062, 1980.

7. J. Doyne Farmer et al. The dimension of chaotic attractors. *Physica*, 7D:153–180, 1983.

8. Michael E. Gaddis and Michael J. Zyda. *The Fractal Geometry of Nature: Its Mathematical Basis and Application to Computer Graphics*. Master's thesis, Naval Postgraduate School, Monterey, California, January 1986.

9. Dino Giuli. Polarization diversity in radars. *Proceedings of the IEEE*, 74 NO. 2, February 1986.

10. Peter Grassberger and Itamar Procaccia. Measuring the strangeness of strange attractors. *Physica*, 9D:189–208, 1983.

11. S.A. Hovanessian. *Introduction to Synthetic Array and Imaging Radars*. Artech House, Inc, 610 Washington St., Dedham, MA, 1980.

12. H. C. Van De Hulst. *Light Scattering By Small Particles*. John Wiley & Sons, Inc, New York, NY, 1957.

13. Alan L. Jones. *Image Segmentation via Fractal Dimension*. Master's thesis, Air Force Institute of Technology, December 1987.

14. Matthew Kabrisky. Human factors engineering class notes. AFIT Fall Quarter 1989.

15. Hiroshi Kaneko. Fractal feature and texture analysis. *Systems and Computers in Japan*, 19, NO. 8, August 1988.

16. Alexander B. Kostinski and Wolfgang-Martin Boerner. On foundations of radar polarimetry. *IEEE Transactions on Antennas and Propagation*, AP-34 NO. 12, December 1986.

17. Benoit B. Mandelbrot. *The Fractal Geometry of Nature*. W.H. Freeman and Company, New York, NY, 1977.

18. James L. Melsa and David L. Cohn. *Decision and Estimation Theory*. McGraw-Hill Book Company, New York, NY, 1978.

19. Dean L. Mensa. *High Resolution Radar Imaging*. Artech House, Inc, 685 Canton St., Norwood, Mass 02062, 1981.

20. James M.Keller et al. Characteristics of natural scenes related to the fractal dimension. *Transactions on Pattern Analysis and Machine Intelligence*, PAMI-9, NO. 9, September 1987.

21. Leslie M. Novak et al. Studies of target detection algorithms that use polarimetric radar data. *IEE Transactions on Aerospace and Electronic Systems*, AES-25 NO. 2, March 1989.

22. Alex P. Pentland. Fractal-based description of natural scenes. *Transactions on Pattern Analysis and Machine Intelligence*, PAMI-6, NO. 6, November 1984.

23. Benjamin Perry and Marvin N. Cohen. Polarimetric pulse compression. In *Pulse Compression Techniques in Radar Systems Professional Program Session Record 7, Electro/84*, Electronic Show and Convention, Boston, MA, May 15-17 1984.

24. August W. Rihaczek. *Principles of High-Resolution Radar*. McGraw-Hill Book Company, New York, NY, 1969.

25. Rudy Rucker. *Mind Tools*. Houghton Mifflin Co, Boston, MA, 1987.

26. Dietmar Saupe. Algorithms for random fractals. In *SIGGRAPH '87, Fractals: Introduction, Basics and Perspectives*, 1987.

27. Mark C. Shelberg et al. Measuring the fractal dimensions of surfaces. October 16 1983. Obtained through DTIC.

28. C.W. Simm et al. On the analysis of experimental signals for evidence of deterministic chaos. *Helvetica Physica Acta*, 60:510–551, 1987.

29. Michael C. Stein. Fractal image models and object detection. *Society of Photo-Optical instrumentation Engineers, SPIE, Visual Communications and Image Processing II*, 845, 1987.

30. James Theiler. Efficient algorithm for estimating the correlation dimension from a set of discrete points. *Physical Review A*, 36 NO. 9, November 1 1987.

31. James Theiler. Estimating fractal dimension. April 26 1989. MIT Lincoln Lab, L-244, P.O. Box 73, Lexington, MA 02173-0073.

32. T. Thompson et al. *NASA/JPL Aircraft SAR Compression Demonstration Tape Information Package*. April 20 1987. Documentation package accompanying JPL SAR data tapes.

33. Kwok Yeung Tsang. Dimensionality of strange attractors determined analytically. *Physical Review Letters*, 57 NO. 12, September 22 1986.

34. Jacob J. van Zyl et al. Imaging radar polarization signatures: theory and observation. *Radio Science*, 22 NO. 4:529–543, July-August 1987.

35. Richard D. Voss. Fractals in nature: characterization, measurement, and simulation. In *SIGGRAPH '87, Fractals: Introduction, Basics and Perspectives*, 1987.

36. Tom Waters. Fractals in your future. *Discover*, March 1989.

37. Donald R. Wehner. *High Resolution Radar.* Artech House, Norwood, MA, 1987.

38. M. W. Whitt and F. T. Ulaby. Millimeter-wave polarimetric measurements of artificial and natural targets. *Proceedings of IGARSS '87 Symposium*, May 18-21 1987. Ann Arbor.

39. Howard J. Zebker et al. Imaging radar polarimetry from wave synthesis. *Journal of Geophysical Research*, 92 NO. B1:683–701, January 10 1987.

Captain Mark A. Maneely ██ entered the Naval Academy Preparatory School in Newport, Rhode Island. He later attended the University of Nebraska-Lincoln, from which he received the degree of Bachelor of Science in Electrical Engineering, with highest honors, in 1983. He received his commission in the USAF as a distinguished graduate of the ROTC program. Before being called to active duty, he worked as a staff engineer at the Air Force Human Resources Laboratory at Williams AFB, Arizona. He then attended flight training at the Euro-Nato Joint Jet Training Program at Sheppard AFB, Texas. He also served as Communication Systems Integration Engineer in Detachment 15, Electronic Systems Division (AFSC), until entering the School of Engineering, Air Force Institute of Technology, in May 1988.

REPORT DOCUMENTATION PAGE		Form Approved OMB No 0704-0188

1a. REPORT SECURITY CLASSIFICATION UNCLASSIFIED	1b. RESTRICTIVE MARKINGS

2a. SECURITY CLASSIFICATION AUTHORITY	3. DISTRIBUTION/AVAILABILITY OF REPORT
2b. DECLASSIFICATION/DOWNGRADING SCHEDULE	Distribution Unlimited

4. PERFORMING ORGANIZATION REPORT NUMBER(S) AFIT/GE/ENG/89D-28	5. MONITORING ORGANIZATION REPORT NUMBER(S)

6a. NAME OF PERFORMING ORGANIZATION School on Engineering A.F. Institute of Tech.	6b. OFFICE SYMBOL (If applicable) AFIT/ENG	7a. NAME OF MONITORING ORGANIZATION

6c. ADDRESS (City, State, and ZIP Code) Wright Patterson, AFB, OH 45433	7b. ADDRESS (City, State, and ZIP Code)

8a. NAME OF FUNDING/SPONSORING ORGANIZATION Wright Research Development Center	8b. OFFICE SYMBOL (If applicable) AARA-2	9. PROCUREMENT INSTRUMENT IDENTIFICATION NUMBER

8c. ADDRESS (City, State, and ZIP Code)	10. SOURCE OF FUNDING NUMBERS			
Wright Patterson, AFB, OH 45433	PROGRAM ELEMENT NO.	PROJECT NO.	TASK NO	WORK UNIT ACCESSION NO.

11. TITLE (Include Security Classification)

FRACTAL GEOMETRY SEGMENTATION OF POLARIMETRIC SYNTHETIC APERTURE RADAR IMAGES

12. PERSONAL AUTHOR(S)
Mark Allen Maneely, Capt, USAF

13a. TYPE OF REPORT MS thesis	13b. TIME COVERED FROM _____ TO _____	14. DATE OF REPORT (Year, Month, Day) 1989 December	15. PAGE COUNT 113

16. SUPPLEMENTARY NOTATION

17.	COSATI CODES		18. SUBJECT TERMS (Continue on reverse if necessary and identify by block number)
FIELD	GROUP	SUB-GROUP	Fractal Geometry, Fractals, Fractal dimension
12	01		Segmentation, Synthetic Aperture Radar
17	09		

19. ABSTRACT (Continue on reverse if necessary and identify by block number)

TITLE: FRACTAL GEOMETRY SEGMENTATION OF POLARIMETRIC
SYNTHETIC APERTURE RADAR IMAGES

Thesis Chairman: David E. Meer
                   Lt Col, USAF

20. DISTRIBUTION/AVAILABILITY OF ABSTRACT ☒ UNCLASSIFIED/UNLIMITED ☐ SAME AS RPT. ☐ DTIC USERS	21. ABSTRACT SECURITY CLASSIFICATION UNCLASSIFIED	
22a. NAME OF RESPONSIBLE INDIVIDUAL Lt Col David E. Meer	22b. TELEPHONE (Include Area Code) (513) 255-3576	22c. OFFICE SYMBOL AFIT/ENG

Abstract

This thesis describes how fractal geometry was used to segment synthetic aperture radar (SAR) images. The fractal dimension of each non-overlapping 8x8 pixel region in a 512x512 pixel image was estimated by use of a multidimensional extension of the box counting algorithm. The differences in estimated fractal dimensions were used to differentiate between regions. The SAR images used were represented by quantized "surfaces". These surfaces were defined by nine different datasets of various Euclidean dimensions ranging from three to five. The degrees of freedom (Euclidean dimensions) of the datasets were the X and Y coordinates of each pixel and various combinations of power return values, magnitude return values and phase return values for each pixel. The SAR return values for four different SAR transmit and receive polarization configurations were determined by polarization synthesis techniques using the Stokes vectors of the transmitted and backscattered waves and the target reflectivity phase matrix. Phase matrix data for three different scenes was provided by the Jet Propulsion Laboratory, Pasadena, CA.

Thesis results indicate that the fractal dimension of an image "surface" provides a useful method to segment SAR images. Comparisons between segmentations made using various datasets indicate that datasets containing the magnitude and phase return values yield more information helpful to image segmentation than do datasets containing only power return values. It was also determined that combinations of the various types of return values (ie. power, magnitude and phase returns) into a single dataset of higher Euclidean dimension, can lead to better segmentations than those made using lower dimensional datasets. The fractal dimension estimation and segmentations techniques used in this thesis are not unique to SAR imagery. They may be easily applied to any data which can be arranged into datasets representing image "surfaces."